

Constraints on turbulent velocity broadening for a sample of clusters, groups and elliptical galaxies using *XMM-Newton*

J. S. Sanders¹, A. C. Fabian¹ and R. K. Smith²

¹ *Institute of Astronomy, Madingley Road, Cambridge. CB3 0HA*

² *MS 6, 60 Garden Street, Harvard-Smithsonian Center for Astrophysics, Cambridge, MA 02138, USA*

16 September 2010

ABSTRACT

Using the width of emission lines in *XMM-Newton* Reflection Grating Spectrometer spectra, we place direct constraints on the turbulent velocities of the X-ray emitting medium in the cores of 62 galaxy clusters, groups and elliptical galaxies. We find five objects where we can place an upper limit on the line-of-sight broadening of 500 km s^{-1} (90 per cent confidence level), using a single thermal component model. Two other objects are lower than this limit when two thermal components are used. Half of the objects examined have an upper limit on the velocity broadening of less than 700 km s^{-1} . To look for objects which have significant turbulent broadening, we use *Chandra* spectral maps to compute the expected broadening caused by the spatial extent of the source. Comparing these with our observed results, we find that Klemola 44 has extra broadening at the level of 1500 km s^{-1} . RX J1347.5-1145 shows weak evidence for turbulent velocities at 800 km s^{-1} . In addition we obtain limits on turbulence for Zw 3146, Abell 496, Abell 1795, Abell 2204 and HCG 62 of less than 200 km s^{-1} . After subtraction of the spatial contribution and including a 50 km s^{-1} systematic uncertainty, we find at least 15 sources with less than 20 per cent of the thermal energy density in turbulence.

Key words: intergalactic medium — X-rays: galaxies: clusters

1 INTRODUCTION

Measurements of the velocity structure of the intracluster medium (ICM) are of great interest. They are important for measuring the turbulence predicted to be injected into clusters from mergers or the accretion of material, tracing how the central nucleus injects energy into its surroundings, examining ICM transport properties, such as looking at metal diffusion or sound waves, and for the determination of cluster gravitational potentials using X-ray observations. However, there are few observational constraints on the amount of bulk flow or random motions within the intracluster medium.

Theoretical models of the intracluster medium have predicted that the fraction of pressure support in gas motions is typically 5 to 15 per cent (e.g. Lau et al. 2009; Vazza et al. 2009). Three-dimensional hydrodynamic simulations typically include at most numerical viscosity, and most do not attempt to examine the effects of magnetic fields on gas motions. Some simulations do however attempt to model the effect of the central active nucleus on the gas motions. Brüggén et al. (2005) predict motions in the range $500 - 1000 \text{ km s}^{-1}$ around the central nucleus. Heinz et al. (2010) finds cluster-wide turbulent line-of-sight velocities of $\sim 500 \text{ km s}^{-1}$ in their simulations of clusters containing AGN jets, examining how easily these signals would be detected by *IXO*.

Turbulent motions have been used to explain the lack of cool X-ray emitting gas in the cores of galaxy clusters. Random motions of $50 - 150 \text{ km s}^{-1}$ could randomize the magnetic field direc-

tion, enhancing conduction and helping suppress central cooling (Ruszkowski & Oh 2010). Turbulence should trigger plasma instabilities, giving thermally stable local heating rates comparable to the cooling rates in the intracluster medium (Rosin et al. 2010; Kunz et al. 2010).

Observational constraints on random turbulent motions in galaxy clusters are mostly indirect in nature. In the elliptical galaxy NGC 4636, Xu et al. (2002) examined the strength of the resonantly scattered 15\AA Fe XVII line relative to the line at 17.1\AA . The ICM can be optically thick in the light of resonant lines given correct temperatures and sufficient densities. Random motions decrease the effect of resonant scattering because the resonant lines are velocity-broadened. Xu et al. (2002) observed the consequences of resonant scattering, inferring that the turbulent velocity dispersion is less than 10 per cent of the sound speed. Werner et al. (2009) also examined this object, concluding a maximum of 5 per cent of energy is in turbulent motions.

Random motions contribute to nonthermal ICM pressure. Churazov et al. (2008) derived the the gravitational mass profiles from optical and X-ray data in M87 and NGC 1399. Stars act as collisionless particles, so comparing their potentials from that derived from X-ray data can measure or place limits on the nonthermal pressure. They obtained an upper limit on the nonthermal pressure of ~ 10 per cent of the thermal gas pressure.

One of the few constraints on turbulence in an unrelaxed

galaxy cluster was made by Schuecker et al. (2004), who examined the power spectrum of pressure fluctuations in the Coma cluster. They deduced that a minimum of 10 per cent of the total pressure in Coma is in the form of turbulence.

The shape of X-ray emission lines provides information about velocity structure in clusters (Inogamov & Sunyaev 2003). The low resolution spectra from CCD instruments can be used to look for changes in bulk velocity as a function of position, if the gain of the instrument is stable enough. Such flows were reported using *ASCA* and *Chandra* in Centaurus (Dupke & Bregman 2001, 2006) and other clusters (Dupke & Bregman 2005). However, Ota et al. (2007) placed an upper limit on bulk flows of 1400 km s^{-1} in the Centaurus cluster using *Suzaku*.

The only direct limit on turbulence in the X-ray waveband came from our recent work examining the *XMM-Newton* Reflection Grating Spectrometer (RGS) spectra from a long observation of the X-ray bright galaxy cluster Abell 1835 (Sanders et al. 2010). Since this cluster is at $z = 0.2523$ and has a compact cool core, the line emission is concentrated in a small region on the sky. The broadening of the emission lines by the slitless RGS spectrometers is therefore small. We were able to place an upper limit on the total broadening, including the turbulent component, of 274 km s^{-1} , at the 90 per cent level. The ratio of turbulent to thermal energy density in the core of Abell 1835 is less than 13 per cent.

In this paper, we continue this work by examining RGS spectra of the most point-like clusters, groups and elliptical galaxies in the *XMM-Newton* archive, to obtain the best current direct limits on turbulent velocity broadening of emission lines.

All uncertainties are at the 1σ level, unless stated otherwise. We use the Solar relative abundances of Anders & Grevesse (1989).

2 ANALYSIS

In the first part of our analysis we measure conservative upper limits on the turbulence in our sample by assuming that the objects are point sources. We measure the total line width of the sources in km s^{-1} , which includes the turbulent component.

As the RGS instruments are slitless spectrometers and the examined objects are not point sources, the spectra are broadened because of the spatial extent of the source in the dispersion direction. The effect of the broadening of the spectrum by the spatial extent of the source is given by

$$\Delta\lambda \approx \frac{0.124}{m} \Delta\theta \text{ \AA}, \quad (1)$$

where m is the spectral order and $\Delta\theta$ is the half energy width of the source in arcmin (Brinkman et al. 1998). This broadening is because when we measure a particular dispersion angle on the detector for an X-ray photon, we cannot differentiate between a change in wavelength and a change in position along the dispersion direction. However, there is a low resolution measurement of the energy of each event by the CCD detector which is used to differentiate the multiple spectral orders, also removing noise and signal from the calibration sources.

The observed broadening of emission lines is the sum of this spatial broadening, the thermal broadening of the ICM and any turbulent motions within the observed region. If we determine what the upper bound is to the broadening of the emission lines, beyond the instrumental point source broadening, subtracting the thermal broadening, we can place an upper limit on the turbulent broadening of the source. In addition we can obtain measurements of the redshift of the objects by measuring the emission line centroids.

It would be useful to be able to remove the broadening due to the source extent. To do this we need to know how the high resolution spectrum of the source varies along the dispersion direction, which is not known. We can estimate how it varies by examining maps of the source properties (temperature, metallicity and abundance) constructed using spatially-resolved spectroscopy of *Chandra* data. These data have much lower spectral resolution than the RGS data, so cannot remove the degeneracies completely. As the RGS gratings and *Chandra* detectors are fundamentally different kinds of instrument, with potential calibration uncertainties, a joint analysis is difficult.

We therefore construct synthetic RGS spectra from *Chandra* spectral maps of several of the sources in the sample. These spectra do not contain any turbulent emission line broadening, but do include spatial and thermal broadening. By measuring the width of the emission lines in these theoretical spectra, and comparing them with the width of the lines in the real spectra, we can identify objects in which there is likely to be significant turbulent velocities.

2.1 Sample selection

The objects we examined were selected on the basis of strong emission lines in order to get good limits on broadening. We examined by eye all the clusters in the *XMM-Newton* archive which came under the category ‘groups of galaxies, clusters of galaxies, and superclusters’ and ellipticals in ‘galaxies and galactic surveys’. We looked for those clusters, ellipticals or groups which had a bright central peak in the EPIC images and emission lines in the preview RGS spectra or when displayed with the *XMM-Newton* online BiRD (Browsing Interface for RGS Data) interface, or gas temperatures where there should be emission lines. The sample is therefore not statistically complete or rigorous and is biased towards bright relaxed objects.

We list the objects in Table 1 and their redshifts taken from the NED database. As the absolute energy calibration for the RGS instruments depends on the source position being correct, we use the X-ray position measurements using *Chandra* if possible. We use the centroid position from the ACCEPT cluster archive (Cavagnolo et al. 2009) if available, verifying the position from *Chandra* data manually to find the X-ray peak. For those clusters without *Chandra* observations we used the *XMM* EPIC peak position.

2.2 Spectral extraction

We downloaded the datasets for each of the clusters listed in Table 1 from the *XMM* archive. We ignored some datasets which were very short or where the lightcurve showed strong flaring. The datasets were processed individually through the RGS RGSPROC pipeline (version 1.28.3, part of SAS 10.0.0). We excluded time periods where the count rate for events with flag values of 8 or 16, on CCD 9, and an absolute cross-dispersion angle of 1.5×10^{-4} (the parameters used in Tamura et al. 2003), was greater than 0.2 s^{-1} .

Foreground spectra were extracted from within 90 per cent of the PSF (point spread function) of a point source, including 90 per cent of the peak of the pulse-height distribution (this is the CCD measurement of energy). The selection region roughly corresponds to a 50 arcsec wide strip across the centre of the cluster. We created spectra for background subtraction from the region outside of 98 per cent of the PSF. Shown in Table 1 are the total cleaned exposure times (summing the RGS1 and RGS2 exposure times) and average foreground and background count rates.

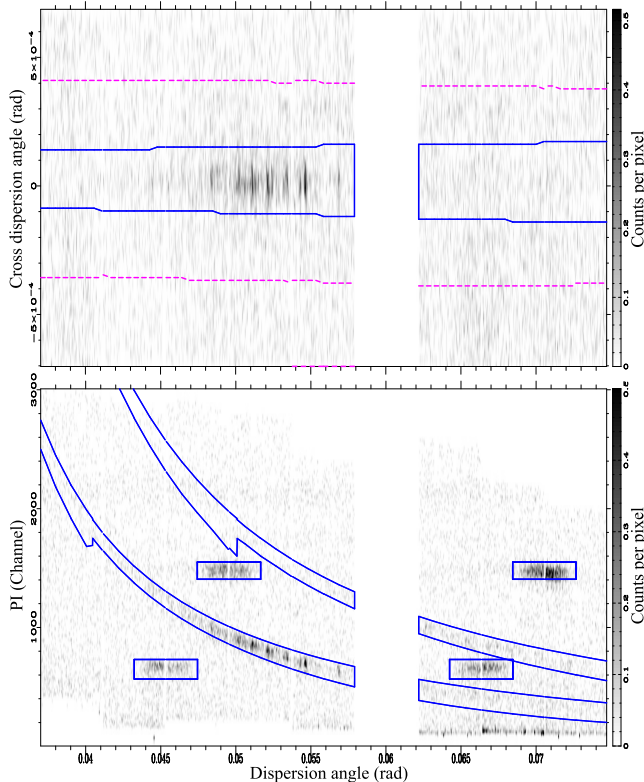


Figure 1. Views of the NGC 4261 0502120101 RGS2 dataset. The bottom panel shows the X-ray events, plotting the CCD-measured energy (PI) against the dispersion angle on the detector. Shown are the first and second order selection regions (corresponding to 90 per cent of the pulse height distribution) and the regions for the calibration sources. The top panel shows those events in the first order spectrum, as a function of dispersion angle and cross-dispersion angle. Within the solid lines are the source extraction region (corresponding to 90 per cent of the width of a point source) and outside the dashed lines are the background extraction region.

The wavelength binning option was used to enable spectral binning by wavelength so that the spectra from the two RGS instruments could be combined. For a particular spectral order and object, we combined the the RGS1 and RGS2 spectra, responses and background files from the appropriate datasets.

We show in Fig. 1 the spectral extraction regions for a line-rich bright source, NGC 4261. The bottom panel shows the dispersion angle of each X-ray event on the RGS2 detector plotted against the PI (pulse invariant) value, which is a measure of the energy of the X-ray photon. The two spectral orders are split up by the pulse height distribution selection. Also seen are the calibration source events, excluded using the rectangles shown. The top plot shows the distribution of the first order events as a function of cross-dispersion direction and dispersion angle.

Some of the most extended objects have background spectra which are contaminated by cluster emission. Fig. 2 shows the background subtraction for Abell 2029 with template backgrounds generated using the SAS RGSBKGMODEL tool and with backgrounds derived from the observation itself. For these extended objects the spectrum from the background region is smoother than the line emission from the centre. This is because this background emission comes from a large part of the cluster, much larger than the core, and is highly broadened.

For Abell 2029 the line width is identical when using a tem-

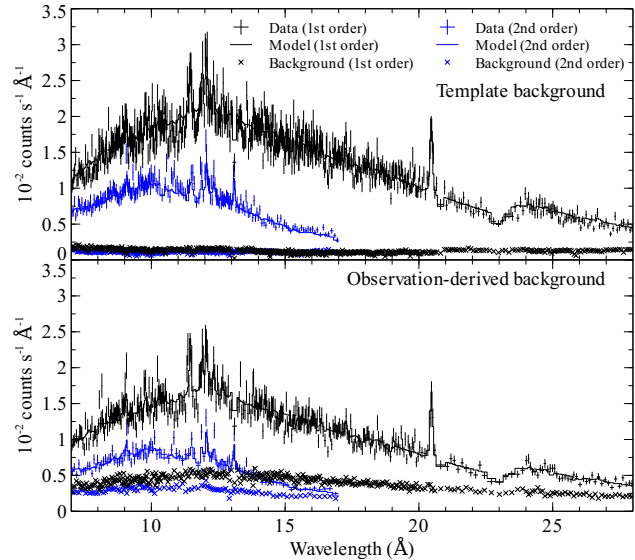


Figure 2. Comparison of background-subtracted data using backgrounds generated from templates (top panel) and from backgrounds from the observation itself (bottom panel) for the extended cluster Abell 2029.

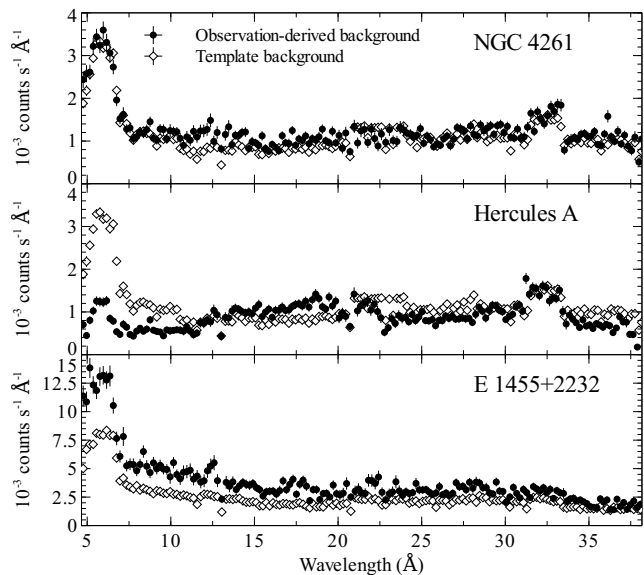


Figure 3. Comparisons of template and observation-derived backgrounds for three observations.

plate background or a background derived from the observation. For some other objects, for example Centaurus, the line width is narrower by $\sim 100 \text{ km s}^{-1}$ using an observation-derived background because the broader component of the emission lines has been subtracted.

We note that our background spectra for several compact objects do not match the template backgrounds generated by the SAS RGSBKGMODEL program, even at wavelengths where the RGS instruments have little effective area. Although some objects such as NGC 4261 (Fig. 3) match the template backgrounds well, others such as Hercules A and E 1455+2232 show substantial mismatches between the templates and observed background at short wavelengths.

2.3 Spectral fitting

For each object we simultaneously fit the spectra with an APEC 1.3.1 spectral model (Smith et al. 2001). In the spectral model we fit the temperature, Galactic absorbing column density, emission measure and abundances for O, Ne, Mg, Si, Fe and Ni. All other elemental abundances were fixed to the have the same ratio relative to Solar as Fe, as their emission lines were weak in the wavelength range examined. The lines in the spectral model were given Gaussian line widths. The width of the lines were the appropriate thermal line widths for an ion at the model temperature, plus an additional velocity width added in quadrature, which was a free parameter in the fits. This additional velocity parameter is of most interest here, as it includes the turbulent broadening and spatial broadening of the object. The redshift of the thermal model is also a free parameter in the spectral fitting.

We simultaneously fit the first order spectra between 7 and 28 Å and second order spectra between 7 and 17 Å, minimising the XSPEC modified Cash statistic when fitting. We used XSPEC version 12.6.0. Using C statistics rather than χ^2 allows us to not bin or group the spectra, helping preserve the energy resolution.

The spectral fitting results are shown in two tables. Table 2 lists the best fitting temperature, column density and metallicities. Table 3 shows the best fitting redshift and 90 per cent upper limit on the line broadening, in km s^{-1} .

Some of the cooler objects are extremely line dominated. For these objects the continuum and emission measure are hard to determine. This leads to large uncertainties on the metallicities, which are measured relative to the continuum. Where the metallicity uncertainties are large, we fix the Fe metallicity to Solar. The other metallicities and emission measures become much better determined when this is done. These objects are listed as having Fe equal to 1 in Table 2.

We show the 90 per cent upper bound on the broadening of the emission line in Fig. 4. These were calculated with the XSPEC error command, which examines how the fit quality changes when a model parameter is stepped over a range of values.

These values are only upper limits because we do not know the effect of the extent of the source in the measurements, which may be the dominant contribution. To show whether the the upper limit is primarily due to the quality of the spectrum or whether the width of the emission line well determined, we also plot the best fitting broadening and its 1σ error bars in Fig. 5. The cumulative distribution of broadening upper limits is shown in Fig. 6. Seven of the objects have upper limits less than 500 km s^{-1} . We show rebinned spectra of these objects in Fig. 7 with their best fitting spectral models. There are also two objects which give limits better than 500 km s^{-1} for a second temperature component added to the model (NGC 4636 and Abell S1101).

To demonstrate how we measure our limits, plotted in Fig. 8 is the change in fit quality as a function of broadening velocity for Zw 3146. The plot shows that for this object we are able to very good limits using either of the spectral orders, or both combined.

For some objects (Abell 262, 2A 0335+096, NGC 4636, Centaurus, Abell 3581, Abell 1991, Abell 2052 and Abell S1101), single component models are poor fits to the spectra. The models do not properly fit the Fe XVII emission lines in the spectrum. For those objects we added a second thermal component to account for the lower temperature gas in the core of the cluster. This cooler component was tied to the same metallicities and redshift as the hotter one. We allowed the cooler component to have a different line broadening. As this cooler material is concentrated in the cores

of these objects it is likely to have a smaller line width because the spatial broadening effect is lower. We show the upper limits for the velocity broadening for the cooler component separately in Table 3 and plot them in Fig. 4.

We looked for other second thermal components in the remaining sample of objects by automatically fitting models. We did not find any objects where the parameters for a second thermal component were distinct from the first component, or where the new line width was well constrained.

2.4 Markov Chain Monte Carlo

Conventional spectral fitting and error estimation can sometimes underestimate the likely range of model parameters which can fit data. An alternative way to determining the model parameter space probability distribution is to use a Markov Chain Monte Carlo (MCMC) method.

We applied the MCMC routine built into XSPEC, which uses the Metropolis-Hastings algorithm to sample parameter space, constructing a chain of parameter values. The algorithm starts from a particular point in parameter space. A new set of parameters is selected by adding values from a proposal distribution (here a N-dimensional Gaussian) to the current parameters. If the quality of fit is better for the new parameters, they are ‘accepted’ and become the next point in the chain. If they have a worse fit, they are accepted randomly with a probability which depends on the increase in the fit parameter. The parameters are otherwise rejected and the next point on the chain is the existing point.

Such a method explores parameter space around the best fit. The fraction of chain values in a particular parameter space region should be related to the likelihood of those model parameters under certain conditions. These include that the proposal distribution should be big enough to explore parameter space (it will take too long to converge if it is too small), but not so large that few points are accepted in a chain. The length of the chain required to sample parameter space depends on factors such as the proposal width and how complex the parameter space is. Unfortunately it is difficult to tell when a chain has sufficiently converged. We manually examined the results of the chain over its run to check that it was covering parameter space randomly and we also checked that the repeat fraction of the chain was close to the rule-of-thumb value of 0.75, which indicates the proposal distribution is correct.

We used the XSPEC MCMC routines to examine the uncertainties on the the broadening of the emission lines for a number of objects. We imposed the following priors on the acceptable range of parameter values:

- (i) The redshift of the object should not vary from the NED value by more than 1500 km s^{-1} .
- (ii) The Galactic column density to the object should not vary from the average values of Kalberla et al. (2005) by more than 20 per cent.
- (iii) Elemental abundances should lie between 0.2 and $1 Z_{\odot}$.

Although these were not necessary for most objects, for some objects the chain wandered into very unlikely regions of parameter space and could not move back. For three objects, Abell 2667, E 1455+2232 and Kelmola 44, we had to impose a fixed redshift on the chain because of the data quality.

We used an initial proposal distribution based on the uncertainties of each parameter using the XSPEC error command. We started the chains from the best-fitting values, discarding the first 2000 values (the burn in period) and using a chain length of 40000

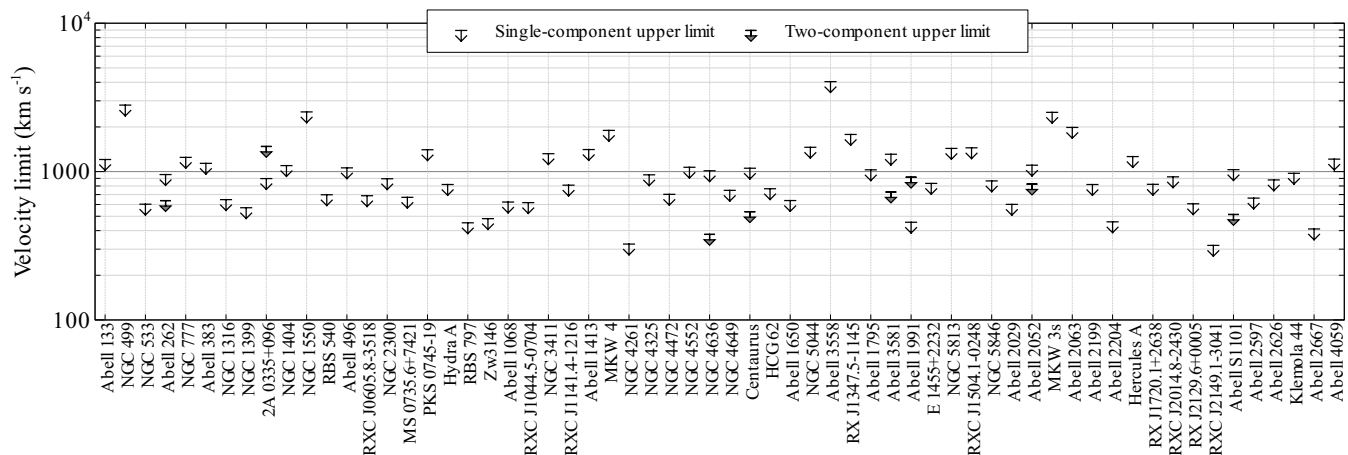


Figure 4. Upper limits (90 per cent) on the turbulent velocity broadening of the spectra. Shown are the limits for single thermal component modelling for all objects, and two temperature modelling for selected objects.

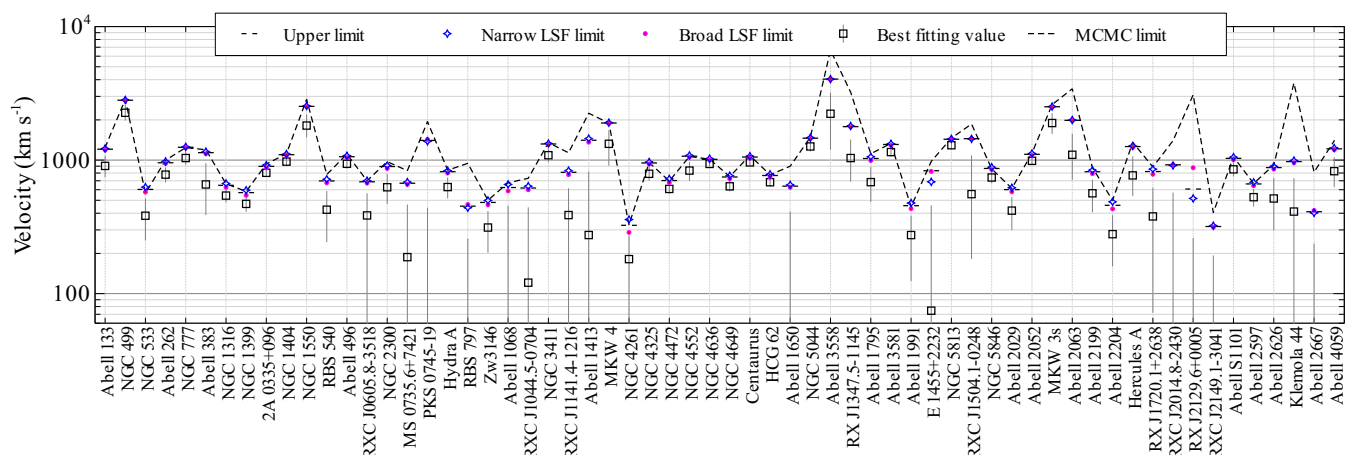


Figure 5. A comparison between the upper limits on the line widths obtained with the standard calibration, and responses in which the LSF is 10 per cent narrower or 10 per cent broader than standard. The continuous line shows the upper limits derived from the MCMC analysis. Also plotted are the best fitting line width and 1σ error bars, which include the spatial component of broadening.

steps. We took the parameter distribution from this chain and used it to create a proposal distribution for a second chain with the same length. We discarded the first chain (used to get a reasonable proposal distribution) and used the second chain to calculate the results. In Fig. 9 are shown the temperature, velocity, redshift and fit statistic as a function of chain step for Zw 3146.

In Fig. 5 are plotted the 90 per cent upper limit from the chains for the velocity broadening, marginalising over the other parameters. We get good agreement between our upper limits and those from conventional spectral fitting for most objects. There are exceptions to this, including RBS 797, RX J2129.6+0005, Abell 2667 and Klemola 44. These objects appear to have a long tail in the marginalised probability distribution for the velocity broadening, often with an inner tighter core. In the case of Klemola 44, the cluster occupies much of the region used to extract spectral backgrounds. If a template background is used instead for this object, the best fitting velocity broadening is 3200^{+950}_{-600} km s⁻¹, close to the limit obtained using MCMC.

2.5 Response line spread function

Fitting the line shape of bright point-like objects such as Capella indicates that systematic uncertainties remain in the line spread function (LSF) of the RGS instruments (den Herder, private communication). If the intrinsic spectral resolution is different from the calibrated value, this would lead to an incorrect determination of the additional line width caused by the extent of the source or motions within the object.

We have approached this problem by adjusting the calibration of the RGS LSF to see the effect on our upper limits. The RGSRM-FGEN response generation tool in SAS supports the use of an optional FUDGE header keyword in the FIGURE part of the RGS1 and RGS2_LINESPREADFUNC.0004.CCF calibration files. This parameter is used to adjust the width of the narrow part of the LSF. We repeated our analysis using values where this width was increased and decreased by 10 per cent, using fudge values of 1.1 and 0.9, respectively.

The upper limits derived using these manipulated line spread functions are also shown on Fig. 4. The effect of this on many ob-

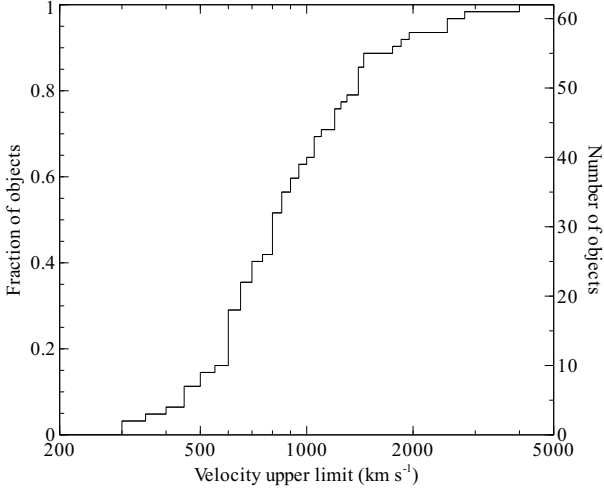


Figure 6. Cumulative distribution of upper limits on velocity broadening, using two temperature component results where appropriate. Note that our sample is highly biased, so this plot should not be used as any indication of the real velocity distribution within clusters or groups. The plot is to indicate the distribution of our results.

jects is small, but can be as much as 50 km s^{-1} for the target with one of the lowest limits, NGC 4261. A typical increase or reduction in the limit is around 25 km s^{-1} . Therefore the effect of the line spread function calibration at the 10 per cent level is relatively small. Any calibration issues are therefore unlikely to change the results by more than 100 km s^{-1} .

3 DIFFERENTIATING SPATIAL BROADENING AND TURBULENCE

Those clusters for which we obtained the best limits on broadening have small compact cores (Fig. 10) and so have low spatial broadening. In order to do better than the limits in Section 2.3 we need to differentiate spatial broadening and intrinsically broad lines, which requires combined spatial and spectral information about the target. We need to know which parts of the RGS spectra come from what dispersion direction angles. This is done by simulating RGS spectra from *Chandra* spectral maps.

3.1 Spectral map creation

Our *Chandra* temperature maps were created by examining the datasets listed in Table 4. The datasets were reprocessed with the standard CIAO tools and very faint event processing was applied if possible. We used an iterative algorithm to remove time periods where the count rate was further than three standard deviations from the median in 200s time bins on the CCDs of the same type which did not include the object itself (ACIS-0, 1 and 2 for ACIS-I observations, and ACIS-5 for ACIS-S observations). We excluded point sources, which were initially detected by WAVDETECT and confirmed by eye.

The Contour Binning algorithm (Sanders 2006) was used to select regions with similar surface brightness containing a minimum signal to noise ratio in each bin (listed in Table 4) between 0.5 and 7 keV. Spectra were extracted from the event files for each of these spatial bins. Background spectra were extracted from blank sky observations, scaled to match the 9 to 12 keV event rate.

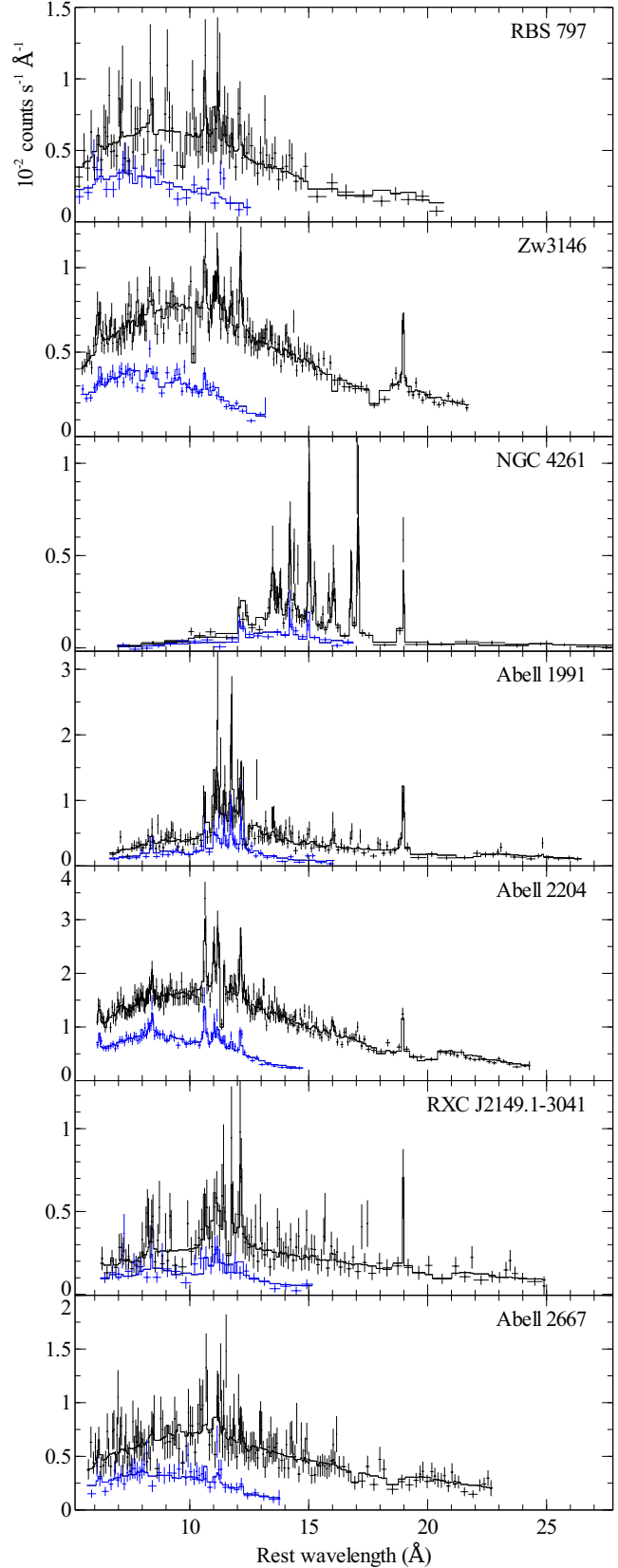


Figure 7. Rebinned combined RGS spectra and best fitting models for the objects where the upper limit on broadening of the emission lines is less than 500 km s^{-1} . The upper and lower data points and models are for first and second order spectra, respectively.

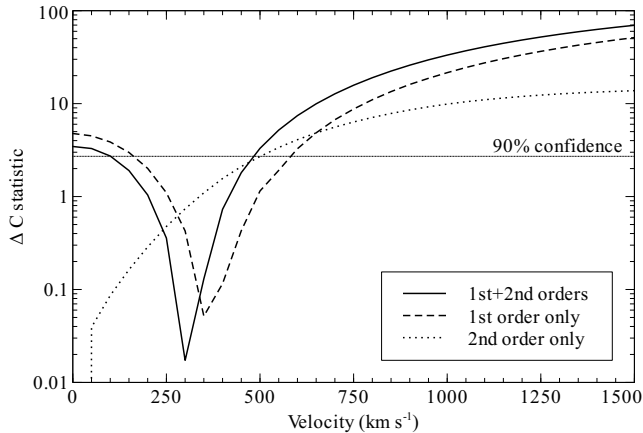


Figure 8. Change in quality of fit as a function of velocity broadening for Zw 3146, fitting both spectral orders or the individual spectral orders. The 90 per cent confidence level is indicated.

We created surface-brightness-weighted response and ancillary response matrices for each bin. When we examined objects with multiple observations, we added the spectra for each bin using the same detector, weighting the response matrices and background spectra according to the relative foreground exposure times.

The spectra were fitted with an absorbed APEC model between 0.5 and 7 keV. The temperature, metallicity and normalization were free in each fit. Solar relative abundance ratios were assumed, and absorption was taken from the Galactic values of Kalberla et al. (2005). Those objects with the best limits have small cool cores (see Fig. 10). For example, Zw 3146 mostly has only temperatures below 4 keV in a 4 arcsec radius region in the core of the cluster. This spatial extent would give a broadening in the Fe-L complex of around $150 - 300 \text{ km s}^{-1}$. Our observed limit is 480 km s^{-1} , which also includes statistical uncertainties.

3.2 Simulating RGS spectra

To assess whether any of our objects have much broader spectra than expected from their spatial extent, we simulated RGS spectra without turbulent broadening using *Chandra* temperature, metallicity and emission measure maps for a subset of our sample. The *Chandra* maps were created using the mapping method above.

For each observation combined in the RGS analysis for an object we deduced which part of the maps were in the RGS extraction region, using the position of the source, rotation angle of the instrument, and the PSF extraction region used. For a particular bin in a map, we calculated the dispersion direction angular distribution of the emission measure per unit area (assuming it was flat over the bin). A response matrix for that bin was then generated using the `angdistset` option to the `RGSRMFGEN` tool, for each detector and RGS order. In `XSPEC` we constructed a spectral model for each bin using the data from the *Chandra* temperature, metallicity and emission measure maps, and simulated spectra using this model and the response matrices for the bin. An absorbed APEC model was used to simulate the spectra, including thermal broadening, but assuming the same abundance ratio of each element to the Solar value. For the simulation an exposure time 100 times greater than the real exposure time for an observation was used. The resulting spectra were then added for each detector and for each spectral order. We then combined the spectra of the same order for all detectors and observations with `RGS COMBINE`, as was done for the real data.

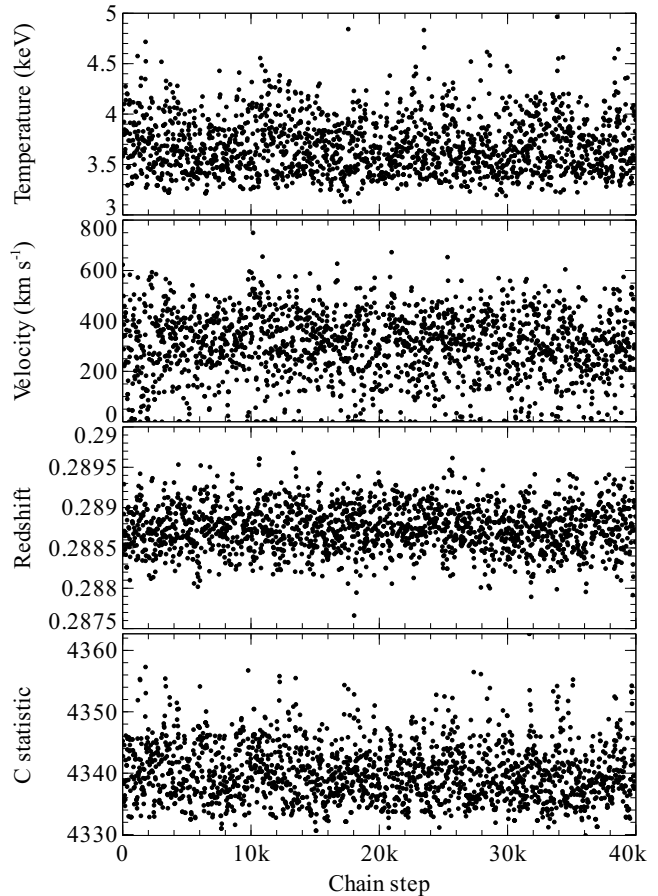


Figure 9. Temperature, velocity, redshift and fit statistic in the MCMC chain for Zw 3146 as a function of the chain step. We plot only 1 out of 20 points for clarity.

These simulated spectra were fit with the same model as we applied to the data to get the expected line broadening from the spatial extent in km s^{-1} . We did not include instrumental or cosmic backgrounds in the simulation and did not produce observationally-derived background spectra in the same way as when extracting the real spectra. The simulated spectra are therefore the whole spectrum from the extraction region. We therefore compare the results here using the real spectra with template blank-sky backgrounds spectra.

There are some weaknesses in this simulation. We do not include our statistical uncertainties in the *Chandra* maps when simulating the spectrum. Solar relative abundances are assumed, however most of the RGS spectral lines are due to Fe and so are the *Chandra* metallicity measurements, so this is probably not a poor approximation except for the O VIII line. We do not account for the cross-dispersion direction change in effective area of the RGS instruments. However, this is small over the 90 per cent PSF extraction region we use. The input maps to the simulation are projected quantities. The RGS and *Chandra* detectors react differently to input radiation, so the projected temperatures may well be different. We do not measure, therefore cannot simulate true-multiphase material inside a bin.

The simulation does relatively well when tested with cool core compact targets. For some hotter targets the simulations have too much of the continuum emission at short wavelengths. In the case of Zw 3146 (Fig. 11), the agreement between our simulations and

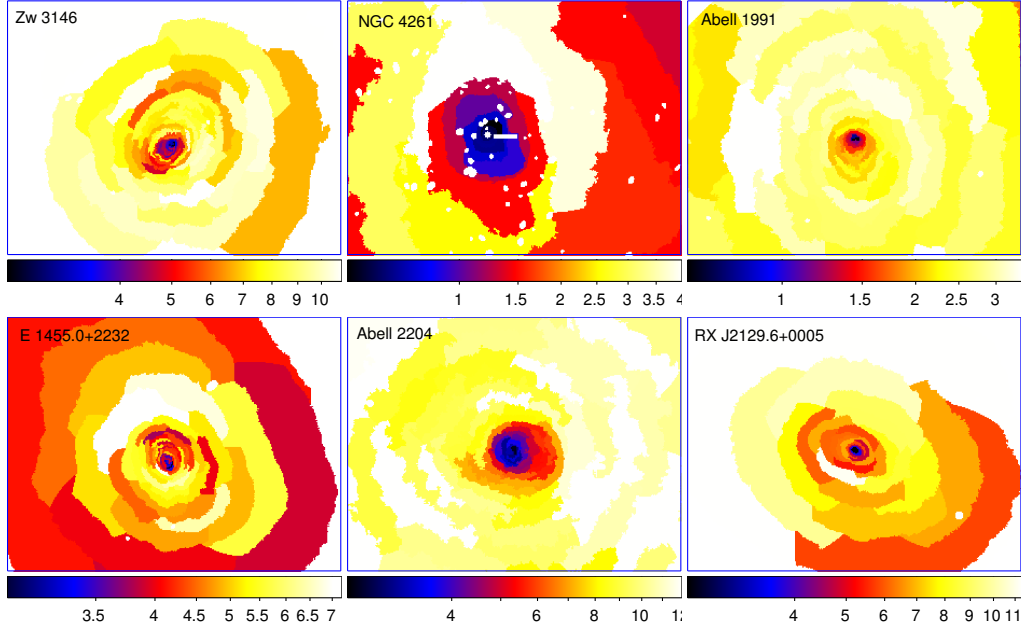


Figure 10. *Chandra* temperature maps for some of the clusters or groups with the lowest broadening limits. The scale below each map is the temperature in keV. Each region is chosen to contain around 900 counts or 2000 in the case of Abell 2204. The maps are at the same scale on the sky, measuring 5 by 3.9 arcmin. Excluded point sources are shown as white regions.

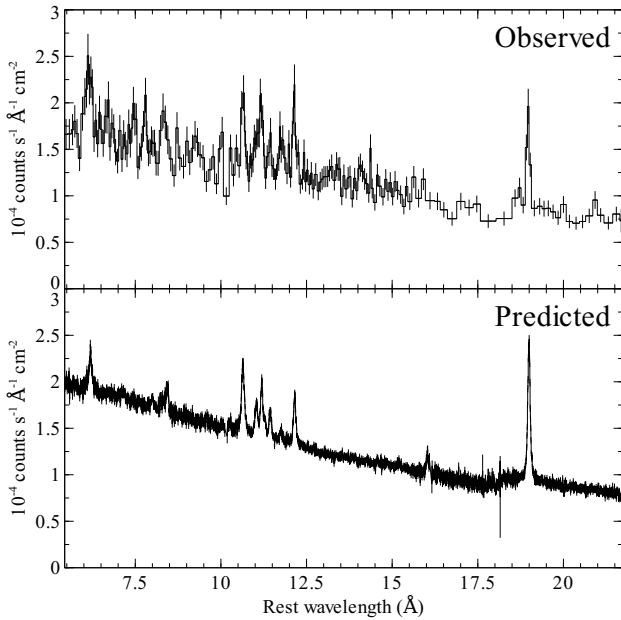


Figure 11. The observed spectra of Zw 3146 and a spectrum simulated using *Chandra* spectral mapping. The observed spectrum was rebinned to have a minimum signal to noise ratio of 10.

the observed spectra at low wavelengths is good. For Abell 1795, the simulation contains 20 per cent more flux at 7\AA than observed. There is reasonable agreement of the line strengths between the real and simulated spectra, however.

Table 5 shows a comparison between the real line widths and measured simulation line widths. We have not included targets where we know there evidence for multiphase gas in the core of the object (e.g. Centaurus, Abell 262 and Abell 3581), as our present

Chandra modelling only fits the spectrum with a single component at each point. For some objects we found there was a discrepancy between the determination of the line widths using standard statistics and using a MCMC analysis. For these we show the MCMC results which tend to be larger (indicated in the table).

There are two objects we have modelled which show evidence for turbulent broadening: Klemola 44 and RX J1347.5-1145. If we take the best fitting model for the Klemola 44 data using a template background, forcing this to have a broadening equal to the that obtained from the simulated spectrum, then we get a C statistic 4.4 higher than the best fitting model. This corresponds to a 3.6 per cent probability of the extra broadening of 1300 km s^{-1} happening by chance. The probability derived using MCMC with a template background, marginalising over the other parameters in the chain, is much lower at 0.7 per cent.

In the case of RX J1347.5-1145, the evidence for an excess broadening is weaker, with a change probability of the increase of 840 km s^{-1} seen by chance of 6 per cent, as calculated from the change in fit statistic. The marginalised probability from the MCMC chains is actually much lower at 0.6 per cent. It is a hot cluster, with a lowest temperature of 5.9 keV in our *Chandra* temperature map, which makes the measurement of emission lines fairly difficult.

Two of the objects show upper limits which are negative (Abell 2597 and NGC 5044). This is clearly unphysical, but we would expect a similar number of negative values given the sample size and that we are using 90 per cent upper limits, if turbulence is intrinsically small. The measured line widths for these objects are close to the predicted values. We note that two-thirds of the objects have predicted line widths greater than their measured values. A 50 km s^{-1} systematic increase in the measured values would give an even balance and remove the two negative upper limits.

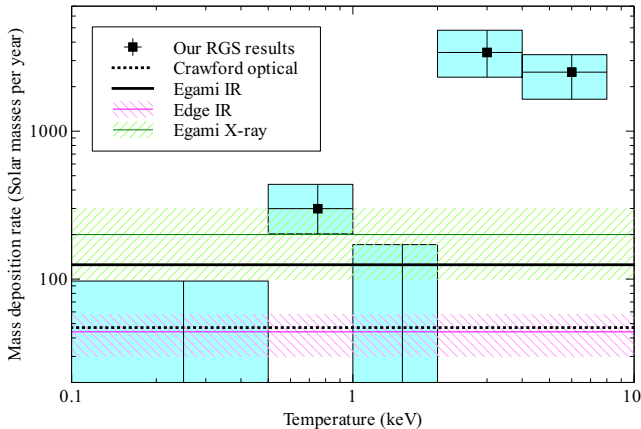


Figure 12. Mass deposition rate as a function of temperature for Zw 3146. The boxes show the 1σ uncertainties on mass deposition rate and ranges or temperature for each component in the model. Also shown are the mass deposition rates from Egami et al. (2006), Edge et al. (2010) and Crawford et al. (1999).

3.3 Zw 3146

Presented in this paper are deep new observations of the luminous galaxy cluster Zw 3146. This adds an additional 176 ks onto the 55 ks of data in the archive. The spectrum for this cluster is shown in Fig. 7 and Fig. 11. Our limit on the broadening of this cluster is 480 km s^{-1} , which is dominated by the spatial extent of the source. If we assume that the expected broadening from the spatial extent from our modelling is correct (Section 3.2), then we are able to convert this to a 90 per cent upper limit on the turbulence of 155 km s^{-1} .

As this is a deep observation we have determined what the distribution on the amount of gas as a function is. As for Abell 1835 (Sanders et al. 2010), we fitted a model made up of gas cooling through ranges of temperature. We use ranges 8 to 4, 4 to 2, 2 to 1, 1 to 0.5 and 0.5 to 0.08 keV. The amount of gas in each bin is parameterized as the mass deposition rate through each temperature range (the number of Solar masses of material which could be cooling radiatively according to the cooling function). We use the best fitting line width and redshift from the previous observation in this analysis and allow the same metals to have free abundances.

The mass deposition rates as a function of temperature are shown in Fig. 12. Also plotted are the Egami et al. (2006) results for cooling rates from *Chandra* and *Spitzer*, Edge et al. (2010) results using *Herschel* and the optical star formation rate from Crawford et al. (1999). Our results are consistent with the observed star formation rates in the optical and infrared wavebands coming from cooling X-ray gas. In the lowest temperature bin our result is below the Egami IR measurement, but this is not statistically significant.

Like in Abell 1835, we find that there is mild evidence for a component at around 0.7 keV in the spectrum, which is equivalent in normalization to a cooling rate of around $300 \text{ M}_{\odot} \text{ yr}^{-1}$.

4 DISCUSSION

4.1 Turbulence

Plotted in Fig. 13 are the upper limits for the sample of objects against RGS temperature. Note that the plotted temperature is measured from the same region as the velocity limit. The central region

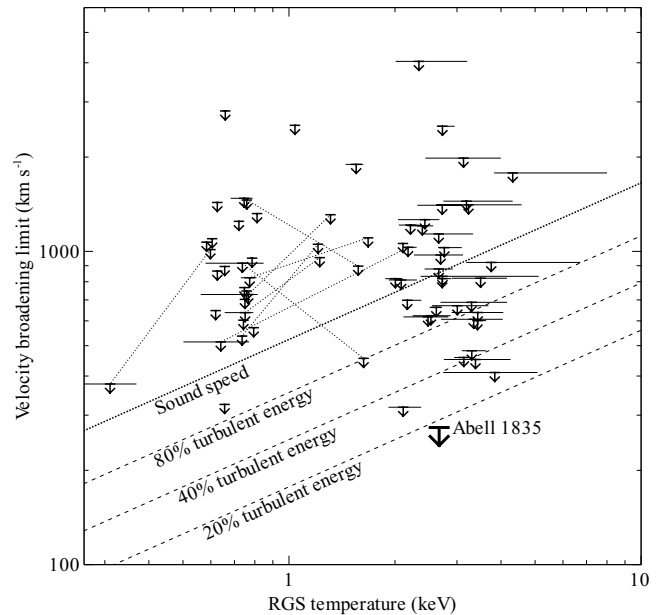


Figure 13. Limits on velocity broadening as a function of RGS-measured temperature. Also plotted are the sound speed as a function of temperature, and what fraction of the thermal energy density the velocity broadening would represent. The points connected by dotted lines show the results using one and two temperature components for the same objects. Abell 1835 is analysed in Sanders et al. (2010).

is likely to be a cool core, and is not the temperature of the bulk of the cluster. We also plot the sound speed as a function of temperature. Shown in addition are lines of constant fractions of turbulent to thermal energy density, calculated using equation 11 from Werner et al. (2009),

$$\frac{\epsilon_{\text{turb}}}{\epsilon_{\text{therm}}} = \frac{V_{\text{los}}^2}{kT} \mu m_p, \quad (2)$$

where V_{los} is the measured line-of-sight velocity, μ is the mean particle mass, m_p is the proton mass and kT is the RGS temperature.

Any trends in this plot should be ignored as the points are upper limits and it is dominated by selection effects. We are able to obtain limits on the broadening less than the sound speed in many objects, and less than half the sound speed in some objects, but unfortunately none of our new limits are better than our previous Abell 1835 limit. The optimal temperature to measure limits relative to the sound speed with the RGS appears to be $\sim 3 \text{ keV}$.

If we make the step of assuming that the spatial contribution to the line widths of the RGS spectra from our simulations are correct (Table 5), we can get better limits for some objects by subtracting the component from the spatial size. Our general result is that there is little evidence for any extra broadening in our spectra due to turbulence. We find typical limits for galaxy clusters with small error bars on the measured results, such as Zw 3146, Abell 496, Abell 1795, Abell 2204 and HCG 62 of only a few hundred km s^{-1} .

Fig. 14 shows the upper limits we obtain after subtracting the contribution from the spatial extent of the source as a function of temperature. Even after including a 50 km s^{-1} additional systematic uncertainty, we find ~ 15 sources which have less than 20 per cent of the thermal energy in turbulence.

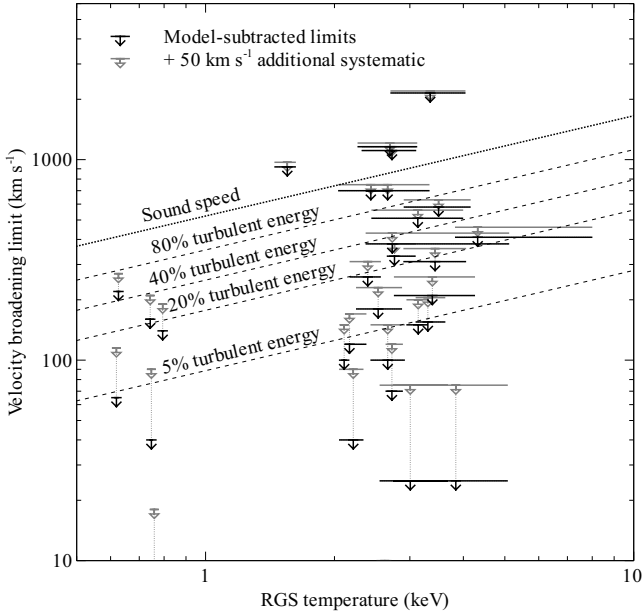


Figure 14. Limits on velocity broadening after subtracting the contribution from the source spatial extent using modelling. These results should be treated with caution as they are dependent on the modelling being correct. We also show the results after adding an additional 50 km s^{-1} possible systematic uncertainty from the LSF calibration.

We find two objects which may have broadening of the emission lines by gas motions. One is Klemola 44, which appears to be turbulently broadened by around 1300 km s^{-1} . The disturbed morphology, lack of a strong central peak and lack of cool core in this object (as seen in our *Chandra* spectral mapping) indicate that it is not relaxed. The cluster hosts a $\sim 60 \text{ kpc}$ long extended radio structure $\sim 40 \text{ kpc}$ from the cluster core (Slee & Roy 1998). This may be a relic indicative of a cluster merger, however, it is smaller and has a steeper radio spectrum than is typical in merger relics, but indicates some sort of major disturbance. In addition the galaxies in the core of the cluster have a much lower velocity dispersion (127 km s^{-1} , Green et al. 1990) than the cluster as a whole (847 km s^{-1}). The core is also offset by around 500 km s^{-1} in mean velocity relative to the surrounding cluster. These observations imply that the cluster has a disturbed velocity structure, agreeing with our findings of line broadening.

The other cluster which hints at turbulent motions at the 840 km s^{-1} level is RXJ1347.5-1145. This object appears to have recently undergone a merger, as seen through X-ray substructure and hot $\sim 20 \text{ keV}$ material in a region only a few 10s of arcsec from the core (Allen et al. 2002; Gitti & Schindler 2004; Miranda et al. 2008; Bradač et al. 2008; Ota et al. 2008). These substructures have also been in Sunyaev-Zel'dovich observations (Komatsu et al. 2001; Mason et al. 2010). Recent lensing and velocity measurements point towards a merger in the plane of the sky (Lu et al. 2010). The cool region in the core of this cluster is only a few arcsec wide, so very good limits would be possible were it not for the large amounts of continuum emission from surrounding gas. Our marginal detection of turbulent broadening in this object is consistent with the merger scenario. Deeper observations of this object could improve the evidence for turbulence.

In order to make better limits or measurements of the turbulence in clusters with *XMM*, observations need to be targeted on

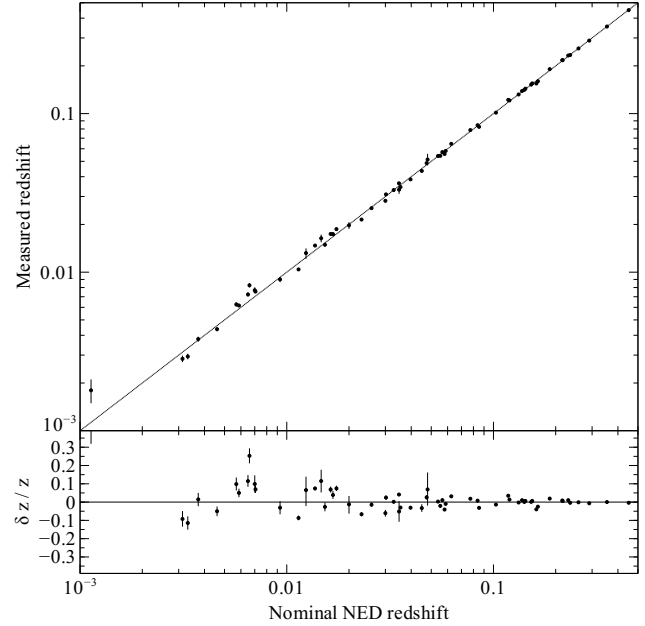


Figure 15. Measurements of redshift compared to the nominal values taken from NED, using single thermal component models. The bottom panel shows the fractional deviation of our measured results from the NED values.

compact bright objects with cool cores at moderate redshift. The flux from emission lines needs to be maximized and the source size minimized, to obtain the best upper limits. In these objects we may become limited by the calibration of the LSF.

The launch of *ASTRO-H* in the future should provide an X-ray calorimeter with energy resolution of $\sim 7 \text{ eV}$ over the 0.3 to 12 keV band. This will revolutionize the measurement of velocities in the intracluster medium. The X-ray microcalorimeter spectrometer on *IXO* in the further future is planned to provide 2.5 eV resolution imaging spectroscopy over the inner $2 \times 2 \text{ arcmin}$ of objects, and 10 eV resolution out to $5.4 \times 5.4 \text{ arcmin}$.

4.2 Redshifts

In Fig. 15 our measured redshifts are plotted against the value from the NED database and the fractional difference as a function of redshift. We show in Fig. 16 the fractional difference between the two values for each object. Although the agreements between our values and those from NED are good in many objects, there are a few targets for which there are a significant discrepancy. This may be due to errors in the analysis, such as problems identifying the position of the centre of the cooler X-ray emitting material if the object is particularly extended. Alternatively they could identify a real velocity difference between the optical and X-ray emission lines. There are no obvious systematic offsets between the NED redshifts and our results.

4.3 Metallicities

We are able to measure the metallicity of several elements in our objects (Table 2). The uncertainty on the metallicities depend quite strongly on temperature because the presence of emission lines is a function of temperature. The absolute metallicities depend on how well the continuum is modelled in the spectral fit. As the extraction regions (a slit) will contain the outer parts of the objects and

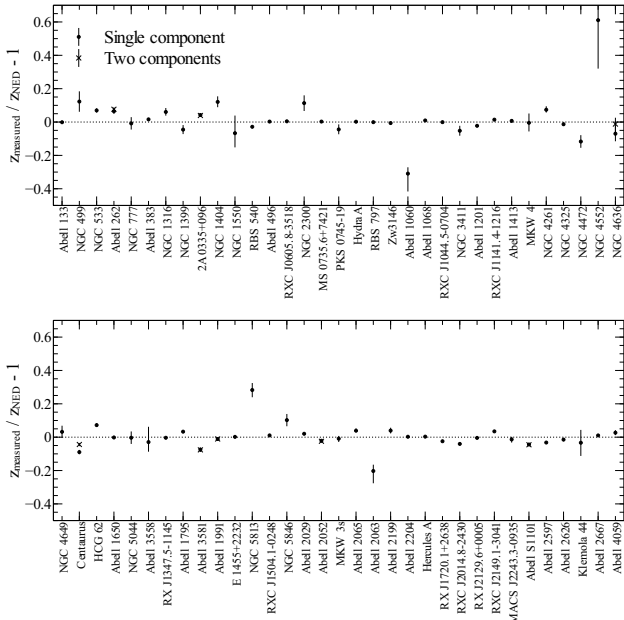


Figure 16. Fractional difference between our measured redshifts and those taken from the NED database. We show the single and two thermal component results as appropriate.

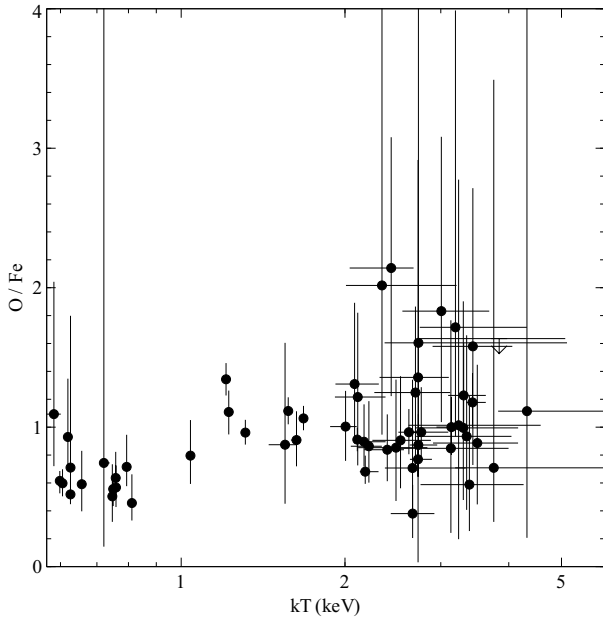


Figure 17. O to Fe ratio, in Solar units, plotted against temperature for the sample. Note that some cooler objects are constrained to have Solar Fe metallicity.

we only use a single temperature model for most of the fits, this can give extra continuum and lower metallicities. Metallicity ratios are more robust than absolute metallicities, especially if there is extra continuum. We plot the O/Fe abundance ratio as a function of temperature for our sample in Fig. 17. We find the Fe/O ratio is similar between the objects and are consistent with Solar. There may be some evidence for lower O/Fe in cooler systems, although our sample has strong selection biases and we are likely to be exam-

ining larger spatial regions in nearby groups than the more distant and hotter clusters.

5 CONCLUSIONS

We examine *XMM-Newton* observations of a sample of galaxy clusters, galaxy groups and elliptical galaxies chosen to have a compact core. By fitting thermal models to their RGS spectra, we place limits on the velocity broadening of their spectra. If we ignore the fact that the objects are extended, we can place conservative upper limits of less than 500 km s^{-1} of broadening for five targets. Half of the objects examined have velocity limits of less than 700 km s^{-1} . After subtracting the spatial component of the broadening by modelling, we find two objects with significant velocity broadening. Klemola 44 which is broadened by around 1500 km s^{-1} and RX J1347.5-1145 by 800 km s^{-1} . In addition, if our modelling of the contribution to the broadening of the spatial extent of the objects is correct, we obtain limits on turbulence for Zw 3146, Abell 496, Abell 1795, Abell 2204 and HCG 62 of less than 200 km s^{-1} . Including a 50 km s^{-1} additional calibration systematic uncertainty, we find 15 sources with less than 20 per cent of the thermal energy density in turbulence.

ACKNOWLEDGEMENTS

ACF thanks the Royal Society for support. We also thank J.-W. den Herder and G. Pratt for useful discussions.

This research has made use of the NASA/IPAC Extragalactic Database (NED) which is operated by the Jet Propulsion Laboratory, California Institute of Technology, under contract with the National Aeronautics and Space Administration.

REFERENCES

- Allen S. W., Schmidt R. W., Fabian A. C., 2002, *MNRAS*, 335, 256
- Anders E., Grevesse N., 1989, *Geochim. Cosmochim. Acta*, 53, 197
- Bradač M. et al., 2008, *ApJ*, 681, 187
- Brinkman A. et al., 1998, in *Proceedings of the First XMM Workshop on Science with XMM*, <http://xmm.esac.esa.int/>
- Brüggen M., Hoeft M., Ruszkowski M., 2005, *ApJ*, 628, 153
- Cavagnolo K. W., Donahue M., Voit G. M., Sun M., 2009, *ApJS*, 182, 12
- Churazov E., Forman W., Vikhlinin A., Tremaine S., Gerhard O., Jones C., 2008, *MNRAS*, 388, 1062
- Crawford C. S., Allen S. W., Ebeling H., Edge A. C., Fabian A. C., 1999, *MNRAS*, 306, 857
- Dupke R. A., Bregman J. N., 2001, *ApJ*, 562, 266
- Dupke R. A., Bregman J. N., 2005, *ApJS*, 161, 224
- Dupke R. A., Bregman J. N., 2006, *ApJ*, 639, 781
- Edge A. C. et al., 2010, *A&A*, 518, L47
- Egami E. et al., 2006, *ApJ*, 647, 922
- Gitti M., Schindler S., 2004, *A&A*, 427, L9
- Green M. R., Godwin J. G., Peach J. V., 1990, *MNRAS*, 243, 159
- Heinz S., Brüggen M., Morsony B., 2010, *ApJ*, 708, 462
- Inogamov N. A., Sunyaev R. A., 2003, *Astronomy Letters*, 29, 791
- Kalberla P. M. W., Burton W. B., Hartmann D., Arnal E. M., Bajaja E., Morras R., Pöppel W. G. L., 2005, *A&A*, 440, 775
- Komatsu E. et al., 2001, *PASJ*, 53, 57
- Kunz M. W., Schekochihin A. A., Cowley S. C., Binney J. J., Sanders J. S., 2010, *arXiv:1003.2719*
- Lau E. T., Kravtsov A. V., Nagai D., 2009, *ApJ*, 705, 1129
- Lu T. et al., 2010, *MNRAS*, 403, 1787
- Mason B. S. et al., 2010, *ApJ*, 716, 739

- Miranda M., Sereno M., de Filippis E., Paolillo M., 2008, MNRAS, 385, 511
- Ota N. et al., 2007, PASJ, 59, 351
- Ota N. et al., 2008, A&A, 491, 363
- Rosin M. S., Schekochihin A. A., Rincon F., Cowley S. C., 2010, arXiv:1002.4017
- Ruszkowski M., Oh S. P., 2010, ApJ, 713, 1332
- Sanders J. S., 2006, MNRAS, 371, 829
- Sanders J. S., Fabian A. C., Smith R. K., Peterson J. R., 2010, MNRAS, 402, L11
- Schuecker P., Finoguenov A., Miniati F., Böhringer H., Briel U. G., 2004, A&A, 426, 387
- Slee O. B., Roy A. L., 1998, MNRAS, 297, L86
- Smith R. K., Brickhouse N. S., Liedahl D. A., Raymond J. C., 2001, ApJ, 556, L91
- Tamura T., den Herder J. W., González-Riestra R., 2003, XMM-SOC-CAL-TN-0034, Technical report
- Vazza F., Brunetti G., Kritsuk A., Wagner R., Gheller C., Norman M., 2009, A&A, 504, 33
- Werner N., Zhuravleva I., Churazov E., Simionescu A., Allen S. W., Forman W., Jones C., Kaastra J. S., 2009, MNRAS, 398, 23
- Xu H. et al., 2002, ApJ, 579, 600

Table 1: List of objects, position used for extraction, nominal redshift, *XMM-Newton* datasets analysed, sum of the RGS1 and RGS2 cleaned exposure times, background-subtracted count rate, and background count rate.

Cluster	RA (J2000)	Dec (J2000)	Redshift	Datasets	Exposure (ks)	Fg. Rate (s^{-1})	Bg. Rate (s^{-1})
Abell 133	01 : 02 : 41.76	−21 : 52 : 49.8	0.0566	0144310101	67.5	0.065	0.026
NGC 499	01 : 23 : 11.65	+33 : 27 : 38.6	0.01467	0501280101	107.8	0.009	0.003
NGC 533	01 : 25 : 31.39	+01 : 45 : 33.1	0.01739	0109860101	68.3	0.019	0.007
Abell 262	01 : 52 : 46.18	+36 : 09 : 10.2	0.0163	0109980101	264.4	0.041	0.019
				0504780101/0201			
NGC 777	02 : 00 : 14.92	+31 : 25 : 45.8	0.016728	0203610301 0304160301	119.0	0.025	0.014
Abell 383	02 : 48 : 03.36	−03 : 31 : 44.7	0.1871	0084230501	64.6	0.037	0.007
NGC 1316	03 : 22 : 41.72	−37 : 12 : 28.3	0.00587	0302780101 0502070201	343.2	0.016	0.006
NGC 1399	03 : 38 : 29.08	−35 : 27 : 02.0	0.0046	0400620101	259.2	0.041	0.015
2A 0335+096	03 : 38 : 41.10	+09 : 58 : 00.7	0.0349	0147800201	267.7	0.152	0.038
NGC 1404	03 : 38 : 51.74	−35 : 35 : 40.4	0.00649	0304940101	74.1	0.048	0.015
NGC 1550	04 : 19 : 37.91	+02 : 24 : 35.8	0.012389	0152150101	61.0	0.043	0.018
RBS 540	04 : 25 : 51.27	−08 : 33 : 36.4	0.0397	0300210401	82.3	0.057	0.017
Abell 496	04 : 33 : 37.86	−13 : 15 : 41.9	0.0329	0135120201	339.1	0.103	0.038
				0506260301/0401			
RXC J0605.8-3518	06 : 05 : 53.98	−35 : 18 : 09.2	0.141	0201901001	73.7	0.049	0.027
NGC 2300	07 : 32 : 19.70	+85 : 42 : 33.3	0.007	0022340201	104.9	0.010	0.005
MS 0735.6+7421	07 : 41 : 44.24	+74 : 14 : 38.2	0.216	0303950101	143.0	0.025	0.010
PKS 0745-19	07 : 47 : 31.19	−19 : 17 : 39.9	0.1028	0105870101	43.3	0.099	0.023
Hydra A	09 : 18 : 05.99	−12 : 05 : 43.9	0.0539	0504260101	244.1	0.139	0.035
RBS 797	09 : 47 : 12.69	+76 : 23 : 13.4	0.354	0502940301	62.9	0.050	0.020
Zw3146	10 : 23 : 39.65	+04 : 11 : 11.2	0.2906	0108670101	426.2	0.064	0.009
				0605540201/0301			
Abell 1068	10 : 40 : 44.52	+39 : 57 : 10.3	0.1375	0147630101	45.5	0.074	0.010
RXC J1044.5-0704	10 : 44 : 32.85	−07 : 04 : 08.7	0.1323	0201901501	57.8	0.058	0.011
NGC 3411	10 : 50 : 26.08	−12 : 50 : 42.5	0.0153	0146510301	71.0	0.052	0.018
RXC J1141.4-1216	11 : 41 : 24.43	−12 : 16 : 39.7	0.1195	0201901601	72.2	0.032	0.019
Abell 1413	11 : 55 : 17.89	+23 : 24 : 21.8	0.1427	0112230501	344.5	0.036	0.017
				0502690101/0201			
MKW 4	12 : 04 : 27.17	+01 : 53 : 44.8	0.02	0093060101/0301	38.2	0.031	0.014
NGC 4261	12 : 19 : 23.23	+05 : 49 : 29.6	0.00706	0502120101	245.0	0.013	0.007
NGC 4325	12 : 23 : 06.62	+10 : 37 : 15.6	0.02571	0108860101	42.6	0.049	0.011
NGC 4472	12 : 29 : 46.78	+08 : 00 : 02.9	0.00332	0200130101	203.7	0.051	0.019
NGC 4552	12 : 35 : 39.82	+12 : 33 : 22.8	0.00113	0141570101	86.8	0.019	0.013
NGC 4636	12 : 42 : 49.92	+02 : 41 : 15.3	0.00313	0111190701	124.4	0.063	0.019
NGC 4649	12 : 43 : 39.95	+11 : 33 : 09.7	0.00373	0502160101	163.9	0.047	0.011
Centaurus	12 : 48 : 48.95	−41 : 18 : 45.0	0.0114	0046340101 0406200101	339.8	0.137	0.050
HCG 62	12 : 53 : 05.71	−09 : 12 : 15.2	0.0137	0112270701	354.7	0.028	0.011
				0504780501/0601			
Abell 1650	12 : 58 : 41.50	−01 : 45 : 44.3	0.0838	0093200101	83.0	0.051	0.019
NGC 5044	13 : 15 : 23.95	−16 : 23 : 07.5	0.00928	0037950101	46.4	0.093	0.032
Abell 3558	13 : 27 : 56.85	−31 : 29 : 44.1	0.048	0107260101	86.1	0.035	0.020
RX J1347.5-1145	13 : 47 : 30.59	−11 : 45 : 10.1	0.451	0112960101	73.8	0.054	0.009
Abell 1795	13 : 48 : 52.36	+26 : 35 : 37.3	0.0625	0097820101	128.7	0.186	0.085
Abell 3581	14 : 07 : 29.78	−27 : 01 : 05.9	0.023	0205990101	375.4	0.064	0.022
				0504780301/0401			
Abell 1991	14 : 54 : 31.62	+18 : 38 : 41.5	0.0587	0145020101	83.7	0.049	0.014
E 1455+2232	14 : 57 : 15.09	+22 : 20 : 32.5	0.2578	0108670201	58.2	0.042	0.025
NGC 5813	15 : 01 : 11.26	+01 : 42 : 07.2	0.0066	0302460101	73.1	0.059	0.018
RXC J1504.1-0248	15 : 04 : 07.42	−02 : 48 : 15.7	0.2153	0401040101	77.8	0.155	0.014
NGC 5846	15 : 06 : 29.35	+01 : 36 : 17.8	0.0057	0021540101/0501	80.9	0.034	0.013
Abell 2029	15 : 10 : 56.14	+05 : 44 : 40.5	0.0773	0111270201	385.7	0.167	0.045
				0551780201/0301/-			
				0401/0501			
Abell 2052	15 : 16 : 44.51	+07 : 01 : 17.0	0.0355	0109920101	417.1	0.090	0.040
				0401520301/0501/-			
				0601/0801/0901/1101/-			
				1201/1601/1701			
MKW 3s	15 : 21 : 51.88	+07 : 42 : 31.8	0.045	0109930101	105.9	0.105	0.039
Abell 2063	15 : 23 : 04.85	+08 : 36 : 20.2	0.034937	0200120401 0550360101	99.6	0.022	0.015
Abell 2199	16 : 28 : 38.27	+39 : 33 : 03.2	0.0302	0008030201/0301/0601	90.1	0.113	0.062
Abell 2204	16 : 32 : 46.96	+05 : 34 : 31.1	0.1522	0112230301	229.5	0.146	0.026
				0306490101/0201/-			
				0301/0401			

Hercules A	16 : 51 : 08.18	+04 : 59 : 32.6	0.154	0401730101/0201/0301	250.0	0.022	0.009
RX J1720.1+2638	17 : 20 : 09.94	+26 : 37 : 29.1	0.164	0500670201/0301/0401	141.0	0.065	0.013
RXC J2014.8-2430	20 : 14 : 51.69	-24 : 30 : 20.5	0.1612	0201902201	53.2	0.078	0.012
RX J2129.6+0005	21 : 29 : 39.94	+00 : 05 : 18.8	0.235	0093030201	113.0	0.039	0.011
RXC J2149.1-3041	21 : 49 : 07.72	-30 : 42 : 04.7	0.1179	0201902601	53.6	0.032	0.008
Abell S1101	23 : 13 : 58.76	-42 : 43 : 34.7	0.058	0147800101	250.9	0.130	0.038
Abell 2597	23 : 25 : 19.78	-12 : 07 : 27.6	0.0852	0108460201 0147330101	275.5	0.109	0.032
Abell 2626	23 : 36 : 30.52	+21 : 08 : 48.2	0.0553	0083150201 0148310101	112.9	0.032	0.012
Klemola 44	23 : 47 : 43.18	-28 : 08 : 34.8	0.03	0204460101	59.6	0.058	0.028
Abell 2667	23 : 51 : 39.40	-26 : 05 : 02.8	0.23	0148990101	61.7	0.064	0.012
Abell 4059	23 : 57 : 01.00	-34 : 45 : 32.8	0.0475	0109950101/0201	108.0	0.046	0.022

Table 2: Spectral fitting results for temperature, column density and metallicities. Uncertainties on values are at the 1σ level. If the Fe metallicity is 1, this means it was fixed at this value in the spectral fit. Column density (n_H) is in units of 10^{20} cm^{-2} . Metallicities are relative to Solar.

Cluster	kT (keV)	n_H	O	Ne	Mg	Si	Fe	Ni
Abell 133	2.39 ± 0.20	< 2	0.70 ± 0.14	$0.71^{+0.31}_{-0.26}$	0.81 ± 0.32	2^{+1}_{-1}	0.83 ± 0.17	1.70 ± 0.96
NGC 499	0.659 ± 0.012	5 ± 4	0.52 ± 0.12	< 0.28	1.69 ± 0.37	< 2	1	2 ± 1
NGC 533	0.743 ± 0.017	7^{+4}_{-3}	$0.70^{+0.18}_{-0.14}$	1.16 ± 0.34	0.87 ± 0.36	< 0.55	1	4 ± 1
Abell 262	1.223 ± 0.020	8.48 ± 0.89	0.313 ± 0.031	0.331 ± 0.070	0.327 ± 0.073	< 0.65	0.282 ± 0.029	1.52 ± 0.20
NGC 777	$0.721^{+0.018}_{-0.011}$	< 13	$0.68^{+0.17}_{-0.36}$	$1.26^{+0.12}_{-0.77}$	1^{+2}_{-1}	< 890	$0.92^{+0.8}_{-0.56}$	4^{+200}_{-3}
Abell 383	$2.66^{+0.67}_{-0.29}$	< 2	$0.30^{+0.19}_{-0.12}$	$0.43^{+0.43}_{-0.23}$	$0.48^{+0.54}_{-0.35}$	$0.73^{+0.47}_{-0.26}$	$0.42^{+0.26}_{-0.11}$	< 0.45
NGC 1316	0.6191 ± 0.0082	2^{+2}_{-1}	$0.251^{+0.072}_{-0.042}$	$0.199^{+0.10}_{-0.055}$	$0.219^{+0.12}_{-0.071}$	12^{+8}_{-4}	$0.270^{+0.094}_{-0.048}$	$0.60^{+0.29}_{-0.17}$
NGC 1399	0.7939 ± 0.0068	9 ± 2	$0.242^{+0.046}_{-0.031}$	$0.351^{+0.12}_{-0.069}$	$0.388^{+0.13}_{-0.079}$	< 5	$0.339^{+0.088}_{-0.049}$	$2.00^{+0.58}_{-0.35}$
2A 0335+096	1.573 ± 0.017	25.44 ± 0.39	0.311 ± 0.023	0.307 ± 0.034	0.287 ± 0.031	0.17 ± 0.15	0.279 ± 0.013	0.371 ± 0.093
NGC 1404	0.6052 ± 0.0079	< 0.18	0.238 ± 0.025	0.324 ± 0.067	0.217 ± 0.083	< 0.56	0.398 ± 0.050	0.80 ± 0.24
NGC 1550	1.040 ± 0.017	13 ± 2	0.294 ± 0.077	0.30 ± 0.18	0.68 ± 0.21	< 1	$0.369^{+0.061}_{-0.025}$	1.92 ± 0.61
RBS 540	$2.168^{+0.21}_{-0.050}$	11 ± 1	$0.485^{+0.10}_{-0.079}$	$0.42^{+0.19}_{-0.15}$	$0.69^{+0.22}_{-0.18}$	2 ± 1	$0.541^{+0.12}_{-0.062}$	0.64 ± 0.52
Abell 496	2.107 ± 0.031	6.37 ± 0.37	0.409 ± 0.029	0.576 ± 0.070	0.505 ± 0.075	< 0.38	0.449 ± 0.026	0.32 ± 0.20
RXC J0605.8-3518	$3.30^{+0.86}_{-0.61}$	5 ± 1	$0.61^{+0.34}_{-0.23}$	$0.87^{+0.58}_{-0.37}$	$0.96^{+0.67}_{-0.44}$	$0.50^{+0.51}_{-0.37}$	$0.62^{+0.45}_{-0.22}$	1^{+2}_{-1}
NGC 2300	0.657 ± 0.015	< 1	0.47 ± 0.12	0.81 ± 0.35	1.06 ± 0.74	< 1	1	3 ± 1
MS 0735.6+7421	$3.01^{+0.68}_{-0.46}$	2 ± 1	$0.68^{+0.27}_{-0.20}$	$0.42^{+0.25}_{-0.20}$	$0.58^{+0.43}_{-0.32}$	$0.50^{+0.29}_{-0.22}$	$0.37^{+0.21}_{-0.12}$	1^{+1}_{-1}
PKS 0745-19	2.73 ± 0.39	39^{+2}_{-1}	< 0.45	0.28 ± 0.13	0.18 ± 0.13	< 0.45	0.158 ± 0.055	< 0.97
Hydra A	$2.724^{+0.17}_{-0.091}$	3.72 ± 0.37	0.235 ± 0.030	0.322 ± 0.066	0.131 ± 0.079	< 0.43	0.305 ± 0.033	< 0.41
RBS 797	$3.39^{+0.87}_{-0.63}$	5 ± 1	$0.19^{+0.14}_{-0.10}$	$0.34^{+0.31}_{-0.21}$	$0.55^{+0.54}_{-0.40}$	$0.32^{+0.29}_{-0.20}$	$0.316^{+0.25}_{-0.057}$	< 0.48
Zw3146	$3.31^{+0.32}_{-0.21}$	3.44 ± 0.49	$0.225^{+0.040}_{-0.034}$	$0.388^{+0.092}_{-0.074}$	0.17 ± 0.11	0.380 ± 0.075	$0.184^{+0.046}_{-0.030}$	0.39 ± 0.34
Abell 1068	$2.53^{+0.35}_{-0.28}$	< 2	$0.271^{+0.10}_{-0.078}$	$0.38^{+0.19}_{-0.14}$	$0.47^{+0.24}_{-0.20}$	0.31 ± 0.20	$0.299^{+0.098}_{-0.074}$	$1.10^{+0.89}_{-0.75}$
RXC J1044.5-0704	2.48 ± 0.36	1 ± 1	$0.211^{+0.098}_{-0.073}$	$0.31^{+0.18}_{-0.13}$	$0.42^{+0.24}_{-0.19}$	< 0.39	0.247 ± 0.076	< 0.34
NGC 3411	0.8117 ± 0.0085	5 ± 2	$0.227^{+0.064}_{-0.050}$	0.19 ± 0.12	$0.79^{+0.36}_{-0.23}$	< 4	$0.497^{+0.18}_{-0.082}$	$2.33^{+0.98}_{-0.54}$
RXC J1141.4-1216	$2.08^{+0.22}_{-0.16}$	2 ± 1	$0.51^{+0.15}_{-0.13}$	$0.65^{+0.32}_{-0.22}$	$0.35^{+0.33}_{-0.28}$	< 0.31	$0.388^{+0.13}_{-0.081}$	< 0.53
Abell 1413	$3.23^{+1}_{-0.62}$	3 ± 1	$0.099^{+0.094}_{-0.064}$	$0.23^{+0.26}_{-0.12}$	$0.34^{+0.32}_{-0.16}$	$0.32^{+0.30}_{-0.16}$	$0.098^{+0.14}_{-0.047}$	< 2
MKW 4	1.552 ± 0.090	< 8	$0.84^{+0.52}_{-0.29}$	$2.25^{+1}_{-0.87}$	< 1	< 17	$0.96^{+0.55}_{-0.33}$	< 2
NGC 4261	0.6565 ± 0.0091	< 1	0.262 ± 0.065	$0.50^{+0.28}_{-0.10}$	0.33 ± 0.17	< 12	$0.442^{+0.14}_{-0.094}$	$1.01^{+0.62}_{-0.30}$
NGC 4325	0.786 ± 0.011	< 3	0.472 ± 0.091	1.42 ± 0.32	1.18 ± 0.29	< 0.62	1	2 ± 1
NGC 4472	0.7499 ± 0.0065	< 1	0.308 ± 0.047	0.67 ± 0.13	0.56 ± 0.12	10 ± 3	0.554 ± 0.071	2.46 ± 0.43
NGC 4552	0.584 ± 0.017	< 4	$0.346^{+0.27}_{-0.084}$	$0.29^{+0.26}_{-0.12}$	$0.83^{+0.70}_{-0.28}$	< 5	$0.316^{+0.13}_{-0.076}$	$1.09^{+0.97}_{-0.44}$
NGC 4636	0.5983 ± 0.0056	< 0.15	0.272 ± 0.029	0.253 ± 0.046	0.345 ± 0.061	< 0.48	0.442 ± 0.034	$1.01^{+0.23}_{-0.16}$
NGC 4649	$0.7580^{+0.011}_{-0.0086}$	< 3	$0.386^{+0.085}_{-0.068}$	$0.57^{+0.17}_{-0.14}$	0.81 ± 0.21	7^{+4}_{-4}	$0.606^{+0.12}_{-0.083}$	2.42 ± 0.59
Centaurus	1.209 ± 0.014	13.04 ± 0.42	0.313 ± 0.017	0.294 ± 0.029	0.255 ± 0.032	< 0.059	0.233 ± 0.016	1.75 ± 0.11
HCG 62	0.7472 ± 0.0079	3^{+3}_{-2}	$0.305^{+0.086}_{-0.071}$	$0.81^{+0.33}_{-0.26}$	$0.61^{+0.27}_{-0.21}$	9^{+7}_{-5}	$0.61^{+0.22}_{-0.17}$	$1.88^{+0.74}_{-0.59}$
Abell 1650	3.44 ± 0.58	< 0.89	$0.37^{+0.20}_{-0.14}$	$0.51^{+0.26}_{-0.20}$	< 0.30	3^{+2}_{-1}	$0.236^{+0.11}_{-0.089}$	< 0.51
NGC 5044	0.7589 ± 0.0097	< 1	$0.317^{+0.070}_{-0.058}$	0.56 ± 0.16	0.81 ± 0.16	< 5	0.559 ± 0.094	2.32 ± 0.51
Abell 3558	$2.34^{+0.87}_{-0.33}$	6 ± 1	$0.41^{+0.25}_{-0.16}$	< 0.26	< 0.53	< 0.39	$0.203^{+0.20}_{-0.075}$	< 0.91
RX J1347.5-1145	$4.32^{+0.52}_{-0.50}$	4 ± 2	$0.21^{+0.16}_{-0.15}$	$0.68^{+1}_{-0.26}$	$0.58^{+1}_{-0.35}$	< 0.68	$0.193^{+0.13}_{-0.085}$	< 7
Abell 1795	$2.76^{+0.33}_{-0.11}$	1.46 ± 0.61	$0.307^{+0.069}_{-0.052}$	$0.553^{+0.16}_{-0.097}$	0.32 ± 0.15	< 0.85	$0.319^{+0.079}_{-0.039}$	0.66 ± 0.47
Abell 3581	1.3120 ± 0.0090	6.42 ± 0.50	0.262 ± 0.020	0.269 ± 0.047	0.319 ± 0.047	< 0.17	0.272 ± 0.014	0.74 ± 0.14
Abell 1991	1.629 ± 0.035	4 ± 1	0.357 ± 0.067	0.33 ± 0.11	0.20 ± 0.13	< 0.31	0.393 ± 0.044	< 0.66
E 1455+2232	$2.73^{+2}_{-0.36}$	< 3	$0.35^{+0.64}_{-0.15}$	< 0.71	< 0.67	< 0.54	$0.217^{+0.72}_{-0.078}$	< 5
NGC 5813	0.6259 ± 0.0073	< 0.41	0.267 ± 0.029	0.301 ± 0.082	0.545 ± 0.094	< 0.59	$0.516^{+0.091}_{-0.045}$	1.37 ± 0.31
RXC J1504.1-0248	$3.19^{+1}_{-0.45}$	9 ± 1	$0.300^{+0.15}_{-0.098}$	$0.30^{+0.35}_{-0.12}$	$0.42^{+0.35}_{-0.16}$	$0.263^{+0.19}_{-0.086}$	$0.175^{+0.22}_{-0.056}$	$1.03^{+1}_{-0.56}$
NGC 5846	0.6260 ± 0.0089	< 0.91	$0.64^{+0.71}_{-0.13}$	$0.80^{+0.90}_{-0.18}$	0.51 ± 0.23	< 4	$0.90^{+0.96}_{-0.17}$	$4.67^{+3}_{-0.73}$
Abell 2029	$3.431^{+0.20}_{-0.085}$	3.23 ± 0.26	0.272 ± 0.032	0.321 ± 0.066	0.341 ± 0.079	$0.85^{+0.60}_{-0.48}$	$0.231^{+0.030}_{-0.020}$	0.94 ± 0.27
Abell 2052	1.678 ± 0.015	6.45 ± 0.40	0.326 ± 0.022	0.355 ± 0.046	0.261 ± 0.052	< 0.083	0.306 ± 0.014	< 0.19
MKW 3s	$2.728^{+0.23}_{-0.099}$	1.51 ± 0.67	0.440 ± 0.080	0.52 ± 0.15	< 0.42	< 0.53	$0.505^{+0.086}_{-0.060}$	< 1
Abell 2063	$3.13^{+0.87}_{-0.69}$	6 ± 2	$0.52^{+0.38}_{-0.27}$	< 1	< 1	< 3	$0.61^{+0.48}_{-0.29}$	< 4

Abell 2199	2.00 ± 0.11	< 1	0.316 ± 0.052	0.38 ± 0.13	0.57 ± 0.16	< 3	0.315 ± 0.059	0.95 ± 0.44
Abell 2204	3.14 ± 0.18	8.05 ± 0.41	0.286 ± 0.045	0.481 ± 0.076	0.373 ± 0.081	0.365 ± 0.069	0.286 ± 0.038	< 0.19
Hercules A	2.43 ± 0.33	7^{+1}_{-1}	$0.51^{+0.16}_{-0.13}$	$0.28^{+0.16}_{-0.13}$	< 0.31	0.46 ± 0.16	0.237 ± 0.078	0.85 ± 0.62
RX J1720.1+2638	3.50 ± 0.63	6^{+1}_{-1}	0.31 ± 0.11	0.32 ± 0.17	0.37 ± 0.21	$0.53^{+0.24}_{-0.20}$	$0.35^{+0.18}_{-0.12}$	2^{+1}_{-1}
RXC J2014.8-2430	$3.75^{+3}_{-0.57}$	12 ± 2	$0.32^{+0.37}_{-0.14}$	$0.61^{+1}_{-0.23}$	< 0.27	$0.24^{+0.48}_{-0.20}$	$0.45^{+1}_{-0.15}$	< 0.75
RX J2129.6+0005	3.35 ± 0.67	2^{+1}_{-1}	$0.241^{+0.13}_{-0.099}$	< 0.21	$0.64^{+0.37}_{-0.30}$	$0.37^{+0.28}_{-0.23}$	$0.26^{+0.15}_{-0.10}$	< 1
RXC J2149.1-3041	$2.11^{+0.26}_{-0.19}$	1 ± 1	0.37 ± 0.12	0.57 ± 0.22	0.59 ± 0.25	$1.07^{+0.68}_{-0.53}$	$0.307^{+0.11}_{-0.079}$	< 0.21
Abell S1101	$2.179^{+0.13}_{-0.049}$	0.82 ± 0.40	$0.258^{+0.032}_{-0.027}$	0.335 ± 0.069	0.271 ± 0.076	0.41 ± 0.24	$0.379^{+0.044}_{-0.028}$	0.55 ± 0.21
Abell 2597	2.62 ± 0.11	1.44 ± 0.39	0.353 ± 0.042	0.52 ± 0.10	0.324 ± 0.096	< 0.13	0.366 ± 0.043	0.47 ± 0.28
Abell 2626	2.66 ± 0.25	2 ± 1	$0.244^{+0.12}_{-0.096}$	0.78 ± 0.29	0.57 ± 0.32	1^{+1}_{-1}	0.64 ± 0.16	2 ± 1
Klemola 44	2.69 ± 0.43	1 ± 1	0.47 ± 0.14	0.30 ± 0.24	< 0.17	< 5	0.38 ± 0.14	< 0.93
Abell 2667	3 ± 1	< 2	$0.20^{+0.23}_{-0.16}$	$0.33^{+0.31}_{-0.22}$	< 0.69	$0.61^{+0.44}_{-0.29}$	$0.32^{+0.37}_{-0.18}$	2^{+2}_{-1}
Abell 4059	2.21 ± 0.15	2 ± 1	0.44 ± 0.10	0.45 ± 0.24	0.29 ± 0.26	< 0.90	$0.51^{+0.14}_{-0.11}$	< 1

Table 3: Upper limits on broadening and redshifts. Shown are measured redshifts for each object (and 1σ statistical errors), the upper limit on the broadening of the emission lines for each object (at the 90 per cent level), the upper limits for cooler component of two temperature model (marked 2T) and the upper limits using response matrices with 10 per cent narrower and broader LSF components.

Cluster	Redshift	Limit (km s^{-1})	MCMC Limit (km s^{-1})	2T Limit (km s^{-1})	Narrow LSF Limit (km s^{-1})	Broad LSF Limit (km s^{-1})
Abell 133	0.05720 ± 0.00051	< 1200	< 1200		< 1200	< 1200
NGC 499	0.01636 ± 0.00091	< 2800	< 2800		< 2800	< 2800
NGC 533	0.01869 ± 0.00025	< 600	< 570		< 630	< 580
Abell 262	0.01742 ± 0.00027	< 960	< 1000	< 640	< 980	< 940
NGC 777	0.01738 ± 0.00036	< 1200	< 1200		< 1300	< 1200
Abell 383	0.19070 ± 0.00089	< 1100	< 1200		< 1200	< 1100
NGC 1316	0.00617 ± 0.00014	< 650	< 660		< 670	< 620
NGC 1399	0.00437 ± 0.00012	< 570	< 580		< 590	< 540
2A 0335+096	0.03634 ± 0.00016	< 900	< 930	< 1500	< 920	< 870
NGC 1404	0.00723 ± 0.00021	< 1100	< 1100		< 1100	< 1100
NGC 1550	0.0132 ± 0.0010	< 2500	< 2900		< 2500	< 2500
RBS 540	0.03848 ± 0.00031	< 700	< 780		< 720	< 680
Abell 496	0.03295 ± 0.00020	< 1100	< 1100		< 1100	< 1000
RXC J0605.8-3518	$0.14110^{+0.00078}_{-0.00063}$	< 690	< 700		< 700	< 670
NGC 2300	0.00769 ± 0.00033	< 890	< 970		< 910	< 870
MS 0735.6+7421	$0.21730^{+0.00059}_{-0.00047}$	< 670	< 830		< 680	< 660
PKS 0745-19	0.10140 ± 0.00061	< 1400	< 1900		< 1400	< 1400
Hydra A	0.05405 ± 0.00030	< 820	< 840		< 830	< 800
RBS 797	0.35410 ± 0.00062	< 450	< 950		< 440	< 460
Zw3146	0.28870 ± 0.00027	< 480	< 500		< 500	< 460
Abell 1068	0.13890 ± 0.00045	< 620	< 680		< 660	< 590
RXC J1044.5-0704	0.13200 ± 0.00053	< 620	< 730		< 640	< 600
NGC 3411	0.01490 ± 0.00037	< 1300	< 1400		< 1300	< 1300
RXC J1141.4-1216	0.12110 ± 0.00053	< 810	< 1100		< 830	< 780
Abell 1413	0.14360 ± 0.00098	< 1400	< 2200		< 1400	< 1400
MKW 4	0.01975 ± 0.00097	< 1900	< 1900		< 1900	< 1900
NGC 4261	0.00755 ± 0.00013	< 320	< 330		< 360	< 290
NGC 4325	0.02534 ± 0.00029	< 950	< 960		< 970	< 930
NGC 4472	0.00294 ± 0.00012	< 700	< 700		< 720	< 680
NGC 4552	0.00180 ± 0.00031	< 1100	< 1100		< 1100	< 1100
NGC 4636	0.00284 ± 0.00013	< 1000	< 1000	< 380	< 1000	< 1000
NGC 4649	0.00379 ± 0.00014	< 750	< 750		< 760	< 720
Centaurus	0.01041 ± 0.00015	< 1100	< 1100	< 540	< 1100	< 1000
HCG 62	0.01472 ± 0.00013	< 770	< 780		< 780	< 750
Abell 1650	$0.08445^{+0.00067}_{-0.00035}$	< 640	< 900		< 650	< 630
NGC 5044	0.00900 ± 0.00033	< 1500	< 1500		< 1500	< 1500
Abell 3558	0.0513 ± 0.0043	< 4000	< 6700		< 4000	< 4000
RX J1347.5-1145	$0.4493^{+0.0022}_{-0.0012}$	< 1800	< 3200		< 1800	< 1800
Abell 1795	0.06447 ± 0.00040	< 1000	< 1100		< 1100	< 990
Abell 3581	0.02147 ± 0.00026	< 1300	< 1300	< 730	< 1300	< 1300
Abell 1991	0.05813 ± 0.00027	< 460	< 450	< 920	< 480	< 430
E 1455+2232	0.25750 ± 0.00084	< 830	< 980		< 690	< 820
NGC 5813	0.00827 ± 0.00027	< 1400	< 1500		< 1400	< 1400
RXC J1504.1-0248	$0.21720^{+0.00083}_{-0.00062}$	< 1400	< 1900		< 1400	< 1400
NGC 5846	0.00626 ± 0.00020	< 870	< 860		< 880	< 850
Abell 2029	0.07872 ± 0.00026	< 600	< 610		< 620	< 580

Abell 2052	0.03443 ± 0.00020	< 1100	< 1100	< 820	< 1100	< 1100
MKW 3s	0.04352 ± 0.00094	< 2500	< 2600		< 2500	< 2500
Abell 2063	0.0331 ± 0.0020	< 2000	< 3400		< 2000	< 2000
Abell 2199	0.03094 ± 0.00036	< 820	< 880		< 840	< 790
Abell 2204	0.15240 ± 0.00020	< 460	< 500		< 490	< 430
Hercules A	$0.15500^{+0.00088}_{-0.00070}$	< 1300	< 1400		< 1300	< 1200
RX J1720.1+2638	0.15990 ± 0.00054	< 820	< 890		< 860	< 780
RXC J2014.8-2430	0.15480 ± 0.00086	< 920	< 1400		< 910	< 920
RX J2129.6+0005	0.23410 ± 0.00051	< 610	< 3100		< 520	< 880
RXC J2149.1-3041	$0.12200^{+0.00046}_{-0.00030}$	< 320	< 400		< 320	< 310
Abell S1101	0.05563 ± 0.00026	< 1000	< 1100	< 510	< 1100	< 1000
Abell 2597	0.08252 ± 0.00023	< 660	< 670		< 680	< 640
Abell 2626	0.05415 ± 0.00057	< 880	< 920		< 900	< 860
Klemola 44	0.02819 ± 0.00055	< 970	< 3800		< 990	< 950
Abell 2667	$0.23240^{+0.00067}_{-0.00055}$	< 410	< 810		< 400	< 420
Abell 4059	0.04873 ± 0.00056	< 1200	< 1400		< 1200	< 1200

Table 4. *Chandra* datasets examined for spectral mapping. Exposure shows the cleaned total exposure time. S/N shows the minimum signal to noise ratio used to create the bins in the binning (square to get the approximate number of counts per bin).

Object	Observations	Exposure (ks)	S/N
Abell 133	2203	34	30
Abell 383	2320, 2321	38	30
Abell 496	931, 3361, 4976	88	40
Abell 1068	1652	26	30
Abell 1650	5822, 5823, 6356, 6358, 7242	164	50
Abell 1795	493, 494, 3666, 5286, 5287, 5288, 5289, 5290, 6159, 6160, 6161, 6162, 6163	91	32
Abell 1991	3193	37	20
Abell 2063	5795, 6262, 6263	41	30
Abell 2204	499, 6104, 7940	97	45
Abell 2597	922 6934 7329	141	30
Abell 2626	3192	24	20
Abell 2667	2214	10	20
Abell 3581	1650	7	15
Abell 4059	897, 5785	129	30
E 1455.0+2232	543, 4192, 7709	108	20
HCG 62	921	48	22
Hercules A	1625, 5796, 6257	112	30
Hydra A	4969, 4970	182	100
Klem 44	4188, 4992	39	30
MKW 4	3234	29	30
MS 0735.6+7421	4197	45	20
NGC 533	2880	36	20
NGC 1316	2022	28	20
NGC 1399	319, 9530	115	40
NGC 4261	834, 9569	134	30
NGC 5044	798, 9399	103	30
NGC 5813	5907, 9517	147	30
PKS 0745-19	508, 2427, 6103, 7694	44	32
RBS 540	4183	10	20
RBS 797	7902	38	20
RX J1347.5-1145	3592	57	30
RX J1720.1+2638	3224, 4361	44	30
RX J2129.6+0005	552, 9370	40	30
Zw 3146	909, 9371	84	30

Table 5. Measured line widths and line widths from spectra simulated using *Chandra* maps in the absence of turbulence. The difference column shows the difference between best fitting velocities of the observed and simulated spectra. The limit column shows the 90 per cent upper limit on the measured velocity after subtracting the predicted velocity. Uncertainties are 1σ in this table. Objects indicated with * show the results using an MCMC analysis.

Object	Real (km s ⁻¹)	Predicted (km s ⁻¹)	Difference (km s ⁻¹)	Limit (km s ⁻¹)
Abell 133	910 ± 170	771 ± 17	140 ± 170	260
Abell 383	670 ± 250	377 ± 26	290 ± 250	700
Abell 496	1050 ± 70	1065 ± 6	-15 ± 70	100
Abell 1068	50 ⁺⁴⁰⁵ ₋₅₀	536 ± 23	-490 ⁺⁴⁰⁵ ₋₅₅	180
Abell 1650*	45 ⁺⁷⁹⁰ ₋₄₅	1034 ± 70	-990 ⁺⁷⁹⁰ ₋₄₅	310
Abell 1795	1040 ± 195	1030 ± 20	10 ± 195	330
Abell 2063	1530 ⁺⁴⁶⁰ ₋₄₀₅	1780 ± 65	-250 ⁺⁴⁶⁰	510
Abell 2204	250 ⁺¹¹⁰ ₋₁₂₅	282 ± 13	-30 ⁺¹¹⁰ ₋₁₂₅	150
Abell 2597	510 ± 75	674 ± 12	-160 ± 75	-40
Abell 2626	705 ⁺²¹⁰ ₋₁₉₀	955 ± 25	-250 ⁺²¹⁰ ₋₁₉₀	100
Abell 2667	0 ⁺²⁴⁰	374 ± 40	-370 ⁺²⁴⁰	25
Abell 4059	1050 ⁺²⁰⁵ ₋₁₇₅	1350 ± 20	-300 ⁺²⁰⁵	40
E 1455.0+2232	0 ⁺⁴⁶⁰	375 ± 33	-375 ⁺⁴⁶⁰	380
HCG 62	710 ± 50	749 ± 4	-40 ± 50	40
Hercules A	770 ⁺³⁰⁰ ₋₂₃₀	573 ± 20	200 ⁺³⁰⁰ ₋₂₃₀	700
Hydra A	750 ± 115	867 ± 12	-120 ± 115	70
Klem 44*	3660 ⁺⁹⁶⁰ ₋₇₂₀	1892 ± 50	2350 ⁺⁹⁶⁰ ₋₇₂₀	1160
MKW 4	1320 ⁺³⁴⁵ ₋₄₁₅	970 ± 20	350 ⁺³⁴⁵ ₋₄₁₅	920
MS 0735.6+7421	300 ± 300	970 ± 40	-470 ± 300	25
NGC 533	530 ± 105	541 ± 8	-10 ± 105	160
NGC 1316	650 ± 60	685 ± 6	-145 ± 65	65
NGC 1399	590 ± 60	545 ± 4	45 ± 60	140
NGC 5044	1530 ⁺¹²⁰ ₋₉₅	1760 ± 16	-230 ⁺¹²⁰ ₋₉₅	-32
NGC 5813	1605 ± 95	1540 ± 6	65 ± 95	220
PKS 0745-19*	910 ⁺⁶⁰⁰ ₋₈₈₀	790 ± 65	120 ⁺⁶⁰⁰ ₋₈₈₀	1110
RBS 540	545 ± 165	700 ± 15	-155 ± 165	120
RBS 797*	0 ⁺⁵³⁵	673 ⁺³⁰ ₋₅₅	-675 ⁺⁵³⁵	210
RX J1347.5-1145*	1320 ⁺⁷⁷⁰ ₋₄₃₀	200 ± 100	1120 ⁺⁷⁷⁰ ₋₄₃₀	410
RX J1720.1+2638	530 ⁺²⁹⁰ ₋₂₅₀	431 ± 25	100 ⁺²⁹⁰ ₋₂₅₀	580
RX J2129.6+0005*	0 ⁺¹⁵³⁰	470 ± 45	-470 ⁺¹⁵³⁰	2150
Zw 3146	310 ± 100	320 ± 10	-10 ± 100	155